arXiv:1401.6091v1 [astro-ph.GA] 23 Jan 2014

January 24, 2014

Selection and Mid-infrared Spectroscopy of Ultraluminous Star-Forming Galaxies at $z \sim 2$

Guanwen Fang[1,2,3], Jia-Sheng Huang[4,5,6], S. P. Willner[6], Xu Kong[1,7], Tao Wang[3,8], Yang Chen[1,9], and Xuanbin Lin[1,7]

jhuang@cfa.harvard.edu, xkong@ustc.edu.cn

ABSTRACT

Starting from a sample of 24 μm sources in the Extended Groth Strip, we use 3.6 to 8 μm color criteria to select ultraluminous infrared galaxies (ULIRGs) at $z \sim 2$. Spectroscopy from 20–38 μm of 14 objects verifies their nature and gives their redshifts. Multi-wavelength data for these objects imply stellar masses $>10^{11}$ $M_\odot$ and star formation rates $\geq$410 $M_\odot$ yr^{-1}. Four objects of this sample observed at 1.6 μm (rest-frame visible) with *HST*/WFC3 show diverse morphologies, suggesting that multiple formation processes create ULIRGs. Four of the 14 objects show signs of active galactic nuclei, but the luminosity appears to be dominated by star formation in all cases.

Subject headings: cosmology: observations — galaxies: starburst — infrared: galaxies — galaxies: high-redshift — galaxies: photometry

[1]Center for Astrophysics, University of Science and Technology of China, Anhui, 230026, China

[2]Institute for Astronomy and History of Science and Technology, Dali University, Yunnan, 671003, China

[3]Key Laboratory of Modern Astronomy and Astrophysics (Nanjing University), Ministry of Education, Nanjing 210093, China

[4]National Astronomical Observatories of China, Chinese Academy of Sciences, Beijing 100012, China

[5]China-Chile Joint Center for Astronomy, Chinese Academy of Sciences, Camino El Observatorio, #1515, Las Condes, Santiago, Chile

[6]Harvard-Smithsonian Center for Astrophysics, 60 Garden Street, Cambridge, MA02138, USA

[7]Key Laboratory for Research in Galaxies and Cosmology, USTC, Chinese Academy of Sciences, China

[8]School of Astronomy & Space Science, Nanjing University, Nanjing 210093, China

[9]Astrophysics Sector, SISSA, Via Bonomea 265, I-34136 Trieste, Italy

1. Introduction

Understanding when and how the most massive galaxies in the universe formed is one of the chief problems in cosmology. A critical redshift era for understanding galaxy formation is $z \sim 2$ or "cosmic high noon" (Grogin et al. 2011). In this era, the cosmic star formation rate density begins to decline from a flat plateau at higher redshifts, the morphological type mix of field galaxies changes, and the number density of quasi-stellar objects (QSOs) peaks. About 50–70% of the stellar mass assembly of galaxies took place in the redshift range of $1 < z < 3$ (Dickinson et al. 2003; Fontana et al. 2003; Steidel et al. 2004; Kong et al. 2006; Richards et al. 2006; Arnouts et al. 2007; Pozzetti et al. 2007; Noeske et al. 2007).

Despite the importance of studying the $z \sim 2$ era, practical identification of galaxies at this redshift using only visible observations is difficult. Visible spectroscopy in particular is greatly hampered because the familiar spectral features shift out of the visible band while the Lyman alpha line has not moved in yet. Nevertheless, there have been some pioneering studies using visible-light selection of galaxies at $z \sim 2$, namely BM/BX sources (Steidel et al. 2004), which are identified using their rest-ultraviolet (UV) absorption lines. Recent near-infrared (NIR) studies have found many more galaxies at $z \sim 2$ with much higher stellar masses and more intensive star formation (Daddi et al. 2004; Labbé et al. 2005; Papovich et al. 2006; Dunne et al. 2009), and infrared (IR) imaging and spectroscopy are essential for studying the whole galaxy population. There are several advantages in studying this galaxy population in the infrared: the NIR bands sample galaxy rest-frame visible spectral energy distributions (SEDs) for galaxies at $z \sim 2$ and thus trace their stellar mass better than rest UV observations can (Cowie et al. 1994), and the mid-IR (MIR)/far-IR (FIR) bands permit measurement of star formation even in very dusty galaxies.

Existing deep NIR surveys have identified massive, passive galaxies already in place at $z \sim 2$, implying that such galaxies formed at even higher redshifts (Franx et al. 2003; Glazebrook et al. 2004; McCarthy et al. 2004; Labbé et al. 2005; Daddi et al. 2005). Based on study of local massive galaxies, the current theoretical view is that massive galaxies are formed through major mergers (Cole et al. 2000; Naab & Burkert 2003; Kormendy et al. 2009). A major merger also triggers the intensive star formation phase known as Ultra-Luminous InfraRed Galaxies (ULIRGs) and feeds gas to central massive black holes to create QSOs (Sanders et al. 1988; Veilleux et al. 2009; Hou et al. 2011)). ULIRGs at $z \sim 2$ have been detected by a variety of methods and are known by many names including Sub-Millimeter Galaxies (SMGs), MIPS 24 μm selected ULIRGs, and Dusty Obscured Galaxies (DOGs) (Chapman et al. 2003; Houck et al. 2005; Yan et al. 2007; Huang et al. 2009; Desai et al. 2009). However, the existence of so many massive galaxies with stellar masses $M_* > 10^{11}$ $M_\odot$ at high redshifts challenges the merger scenario for the formation of massive

galaxies. Current numerical simulations (e.g., Narayanan et al. 2009) have failed to produce as many major mergers as required to explain the observed number of ULIRGs at $z \sim 2$. Davé et al. (2010) proposed an alternative formation scenario for SMGs: a massive gas-rich galaxy could have star formation rate (SFR) as high as 180–500 $M_\odot$ yr^{-1} without any merging process, implying that ULIRGs at $z \sim 2$ with L_{IR} just above 10^{12} $L_\odot$ may have a different formation mechanism than more luminous ULIRGs. A complete census of ULIRGs over the full luminosity range is needed to solve the puzzle of massive galaxy formation at $z \sim 2$.

Morphological studies can elucidate the ULIRG formation process by showing the presence or absence of merger signatures. Recent morphological studies (Dasyra et al. 2008; Melbourne et al. 2008, 2009; Bussmann et al. 2009, 2011; Zamojski et al. 2011; Kartaltepe et al. 2012) using high-angular-resolution NIR images have shown that $z \gtrsim 2$ ULIRGs exhibit a wide range of forms from unresolved to complex structures and sometimes but not always multiple components. The diversity of morphologies indicates that ULIRGs may occur in different interaction stages of major mergers, in minor mergers, or via secular evolution not involving mergers at all.

Most ULIRGs are so optically faint that they were recognized as a class only when infrared satellite surveys became available. The optical faintness is because the UV-optical emission is absorbed by dust and re-emitted in the far-infrared (Sanders & Mirabel 1996). Therefore infrared surveys are needed to give unbiased samples of ULIRGs. Redshift surveys of SMGs (Chapman et al. 2003) have revealed a much larger ULIRG population at $1.7 < z < 2.8$ than at $z \approx 0$. SMGs, however, represent a selection method known to be biased toward low dust temperature systems. In contrast, Magdis et al. (2010) showed that selecting a sample based on MIPS 24 μm sources with IRAC 3.6–8 μm colors indicating that the 1.6 μm stellar "bump" is near 4.5 μm (Huang et al. 2009) produced a $z \sim 2$ ULIRG sample having a wide range of dust temperatures.

This paper defines a lower luminosity sample of $z \approx 2$ ULIRGS and examines their properties, including using *HST*/WFC3 NIR images to examine morphologies. The study is enabled by the data release of the EGS region of the Cosmic Assembly Near-IR Deep Extragalactic Legacy Survey (CANDELS: Grogin et al. 2011; Koekemoer et al. 2011). The CANDELS survey covered ∼210 arcmin^2 with a total exposure time in the EGS of 90 HST orbits. The survey reaches 5σ point-source depth of $H_{AB} \sim 26.5$ at resolution (measured from PSF FWHM) of 0.″12–0.″18. The NIR data are complemented by I (F814W) data having resolution 0.″08–0.″09 from *HST*/ACS. (Pixel scales are 0.″03/pixel in ACS and 0.″06/pixel in WFC3.)

Infrared spectroscopic ULIRG surveys are particularly valuable. In addition to giving redshifts, MIR spectra of ULIRGs divide the objects into two types. Ob-

jects with strong power-law continua are powered mainly by active galactic nuclei (AGNs) (Roche, Whitmore, Aitken, & Phillips 1984; Houck et al. 2005; Sajina et al. 2007; Weedman et al. 2006; Dasyra et al. 2009), while those with strong polycyclic aromatic hydrocarbon (PAH) emission are powered by intensive star formation (Roche & Aitken 1985; Weedman et al. 2006; Farrah et al. 2008; Dasyra et al. 2009; Desai et al. 2009; Huang et al. 2009; Fadda et al. 2010; Fiolet et al. 2010). At $z \sim 2$, the MIPS 24 μm band probes rest-frame $\lambda \sim 8$ μm where there is a strong PAH emission feature. This means samples selected at 24 μm will be especially effective in finding star-forming ULIRGs.

Most work on $z \sim 2$ ULIRGs has concentrated on objects with $L_{\rm IR} > 10^{12.5}$ (Houck et al. 2005; Weedman et al. 2006; Yan et al. 2007; Farrah et al. 2008; Desai et al. 2009; Huang et al. 2009; Fiolet et al. 2010). This paper is instead a study of a lower-luminosity sample of 14 ULIRGs with $10^{12.0} < L_{\rm IR} < 10^{12.6}$. Section 2 of the paper describes the sample selection. The IRS spectroscopic results are presented in Section 3, and Section 4 analyzes stellar populations, SFRs, stellar masses (M_*), total infrared luminosities ($L_{\rm IR}$), morphologies, and AGN fraction. Finally, a brief summary is presented in Section 5. All magnitudes and colors are in the AB system, and notation such as "[3.6]" means the AB magnitude at wavelength 3.6 μm. The paper uses cosmological parameters $h \equiv H_0[\mathrm{km\ s^{-1}\ Mpc^{-1}}]/100 = 0.71$, $\Omega_\Lambda = 0.73$, $\Omega_{\rm M} = 0.27$.

2. Sample Selection

For the present study, IRS targets were selected from the 24 μm sources (Papovich et al. 2004) in the Extended Groth Strip (EGS) region, where the survey was more than 80% complete for $F(24\ \mu\mathrm{m}) > 0.11$ mJy. Huang et al. (2009) presented IRS spectroscopy for a 24 μm sample with $F(24\ \mu\mathrm{m}) > 0.6$ mJy and obtained a narrow redshift distribution at $z \sim 1.9$. For this paper, we selected a fainter sample of 14 objects with $0.2 < F(24\ \mu\mathrm{m}) < 0.6$ mJy. Most objects in our sample have $0.2 < F(24\ \mu\mathrm{m}) < 0.5$ mJy with only two having $0.5 < F(24\ \mu\mathrm{m}) < 0.6$ mJy.

In the redshift range of $1.4 < z < 2.7$, the four IRAC bands (3.6–8.0 μm) probe the rest-frame NIR bands where nearly all galaxy stellar population SEDs have similar shapes. In particular, the rest 1.6 μm stellar emission peak is nearly always present independent of redshift or metallicity. As described by Huang et al. (2009), at $z < 1.4$, the IRAC 3.6 and 4.5 μm bands sample the Rayleigh-Jeans tail of stellar emission resulting in $[3.6] - [4.5] < 0$, while at $z > 1.4$, the 1.6 μm bump moves beyond the IRAC 3.6 μm band, and $[3.6] - [4.5] > 0$. These properties make color selection with IRAC comparable to BzK (Daddi et al. 2004) selection in completeness and contamination (Sorba & Sawicki 2010),

and Huang et al. (2004) and Papovich (2008) have used IRAC color to select galaxies at $z > 1.4$. A limitation of the technique is that very dusty galaxies can have $[3.6] - [4.5] > 0$ even at $z < 1.4$. We therefore propose to use $[5.8] - [8.0] < 0$ to exclude dusty galaxies and also AGNs with power-law-like SEDs. This cut also excludes galaxies at $z \gtrsim 2.7$ because the 1.6 μm bump begins to move past the 5.8 μm band. Therefore the adopted color criteria for our faint 24 μm sample for IRS spectroscopy are:

$$[3.6] - [4.5] > 0 \quad \& \quad [5.8] - [8.0] < 0. \tag{1}$$

These color criteria select galaxies in the redshift range of $1.4 \lesssim z \lesssim 2.7$ as illustrated in Figure 1. Throughout this redshift range, the 7.7 μm PAH emission feature is within the wavelength coverage of the IRS, enabling redshift measurements. Huang et al. (2009) used a similar selection

$$0.05 < [3.6] - [4.5] < 0.4 \quad \& \quad -0.7 < [3.6] - [8.0] < 0.5, \tag{2}$$

but using a fourth IRAC wavelength (5.8 μm) as in criteria (1) does a better job of rejecting galaxies with near-power-law SEDs because all power laws lie outside the criteria (1) selection while some (those with ($-0.6 \lesssim \alpha \lesssim -0.2$ for $F_\nu \propto \nu^\alpha$) lie inside criteria (2).

Figure 2 compares criteria (1) with other selection methods, which all effectively select galaxies at $z \sim 2$. However, only the IRAC selection uses the rest-frame NIR bands, making the sample selection nearly unaffected by dust reddening. Moreover, NIR emission is closely tied to stellar mass (Bell & de Jong 2001), and the resulting sample is therefore roughly equivalent to a stellar-mass-selected sample. It is thus ideal for studying luminous, massive galaxies (Huang et al. 2004; Conselice et al. 2007). As expected, 24 μm sources show a range of IRAC colors, but Figure 3 shows that one dense concentration is in the region cornered by criteria (1). The present sample consists of 11 objects with $0.2 < F(24\ \mu\mathrm{m}) < 0.6$ mJy and satisfying criteria (1)[1] and 3 X-ray sources (EGS25/EGS27/EGS34) with colors satisfying the criteria in Huang et al. (2009) for comparison. The positions and flux densities for objects in the sample are listed in Table 1.

There are many IRS surveys for IR luminous sources at $z \sim 2$ using samples with differing criteria (Weedman et al. 2006; Yan et al. 2007; Farrah et al. 2008; Desai et al. 2009; Huang et al. 2009). When color selection is used, there are two general categories of selection

[1]One object, EGS6, was initially selected with criteria (1) and observed with IRS. After the IRS observation, the EGS IRAC images and catalog were updated with new IRAC imaging from the *Spitzer* GO program 49888 (PI: Nandra). The updated color for EGS6 became $[5.8] - [8.0] = 0.05$, slightly too red to qualify per criteria (1), but we include this source nevertheless.

criteria: DOGs selected by very red visible to infrared colors and galaxies selected in the infrared with SEDs peaking at $\gtrsim$4.5 μm. Table 2 summarizes selection criteria for the relevant IRS surveys, and Figure 3 shows how the various samples compare with criteria (1). Houck et al. (2005) used a selection of the first type: MIPS 24 μm-luminous sources very faint at visible wavelengths. Objects of this type show strong MIR continua with $[5.8]-[8.0]$ colors much redder than the majority of 24 μm sources, strong silicate absorption, and weak or absent PAH emission features. Similar types of objects observed by other groups (Weedman et al. 2006; Yan et al. 2007) yield similar results. The strong power law continua and weak or absent PAH emission features show that these sources are AGNs. However, fainter sources (median $F(24\ \mu\mathrm{m}) = 0.18$ mJy) selected by the DOG criterion (Pope et al. 2008) are predominantly star forming. Selection via IRAC colors (Weedman et al. 2006; Farrah et al. 2008; Desai et al. 2009; Huang et al. 2009) finds objects whose MIR spectra show strong PAH emission features, indicating that star formation powers their FIR emission. When all existing spectra are used to categorize sources, 90% of SB-dominated objects meet criteria (1), though this result is biased by the initial sample selections.

3. IRS Observations and Data Reduction

IRS observations of our sample were made as part of the GTO program for the *Spitzer*/IRAC instrument team (program ID: 30327). Objects were observed with the IRS Long-wavelength Low-resolution first order (LL1) mode with wavelength coverage 20–38 μm and slit width $10\farcs7$. For galaxies at $z \sim 2$, major spectral features including the PAH emission features at 7.7, 8.6, and 11.3 μm and silicate absorption from 8 to 13 μm (peaking at 9.7 μm) fall in the observable wavelength range. IRS observation of each object consisted of 6 exposures with ramp duration 120 s. Mapping mode (Teplitz et al. 2007) was used, offsetting the pointing by $24''$ along the IRS slit between exposures. This mode not only gives more uniform spectra for the targets but also better rejects cosmic rays and bad pixels. All spectra were processed initially with the *Spitzer* Science Center pipeline version 13.0. Extraction of source spectra was done with both the `SMART` analysis package (Higdon et al. 2004) and customized software (Huang et al. 2009) to produce calibrated spectra.

Figure 4 shows the IRS spectra of the 14 sources in our sample. All objects in the sample show PAH emission features at 7.7, 8.6, 11.3 μm in their spectra, and some have silicate absorption at 9.7 μm. We measured redshifts by cross-correlating the observed spectra with two local templates, M82 and Arp 220. The two templates yield very nearly the same redshifts with a typical difference of $\Delta z = 0.02$. The M82 template fits all spectra better. Figure 5 shows the redshift distribution of our sample compared with some works

from the literature. Our sample all lies within $1.6 < z < 2.4$ (Table 3), demonstrating the efficiency of our selection criteria. The three X-ray sources have spectra generally similar to the rest of the sample. EGS25 and EGS27 have weaker silicate absorption and higher continuum than most sources, consistent with their red $[5.8]-[8.0]$ colors in Figure 3. EGS34, however, has strong silicate absorption and weak PAH emission.

Figure 5 shows that the redshift distribution of our sample is very similar to that of the SB-dominated ULIRGs selected with higher limiting flux densities (Farrah et al. 2008; Desai et al. 2009; Huang et al. 2009; Fadda et al. 2010; Fiolet et al. 2010). The narrow redshift distribution for the ULIRGs is due to the selection of strong 7.7 μm PAH emission by the MIPS 24 μm band at $z \sim 1.9$. The mean redshift of 114 ULIRGs in the various surveys is $\langle z \rangle = 1.89$ with a dispersion $\sigma = 0.25$. Our sample has $\langle z \rangle = 1.95$ and $\sigma = 0.19$. On the other hand, luminous 24 μm sources with power-law SEDs have a much wider redshift range extending from $z \sim 0.5$ to $z \sim 3$ (Houck et al. 2005; Weedman et al. 2006; Yan et al. 2007).

4. Multi-Wavelength Studies of ULIRGs at z∼2

AEGIS (All-wavelength Extended Groth Strip International Survey) is a multi-wavelength survey covering X-ray to FIR bands in the Extended Groth Strip area (Davis et al. 2007).[2] The rich multi-wavelength data permit the study of SEDs and physical properties for objects in our sample. MIR and FIR photometry for this sample is particularly important in determining their properties. All but the three X-ray sources were detected by *AKARI* at 15 μm. One object (X-ray source EGS34) was detected at 70 μm in the FIDEL survey. The three X-ray-selected objects and EGS22 were detected in the *Chandra* 800 ks X-ray imaging (Laird et al. 2009). Four objects in our sample, EGS6/EGS9/EGS25/EGS34, are in the VLA 1.4 GHz radio catalog (Ivison et al. 2007; Willner et al. 2012). Figure 7 shows SEDs of the sample galaxies.

4.1. Total Infrared Luminosity and Star Formation Rate

FIR luminosity is an important measurement in characterizing ULIRGs at $z \sim 2$. ULIRGs with different $L_{\rm IR}$[3] and thus different SFRs may have undergone different for-

[2]AEGIS data products are described at http://aegis.ucolick.org/astronomers.html , and data are included in the "Rainbow" data compilation at https://rainbowx.fis.ucm.es/Rainbow_Database/Home.html .

[3]We adopt the Sanders & Mirabel (1996) definition of $L_{\rm IR} \equiv L(8\,\mu{\rm m} - 1\,{\rm mm})$.

mation processes. ULIRGs may be the dominant contribution to star formation density at $z \sim 2$ (Lagache et al. 2004; Caputi et al. 2007), making them especially important to characterize. Direct measurement of $L_{\rm IR}$ requires FIR ($\sim$100 μm) photometry, which can sample the peak of the dust emission SED, but FIR photometry is not yet available for most of the sources. Many groups have made substantial efforts to convert MIR luminosities into $L_{\rm IR}$ (Chary & Elbaz 2001; Reddy et al. 2006; Caputi et al. 2007; Bavouzet et al. 2008; Rodighiero et al. 2010; Wu et al. 2010), but the results remain uncertain.

In order to estimate SFR, we derived $L(8\ \mu{\rm m})$ for our sample from the observed 24 μm flux densities. At $z \sim 2$, 24 μm corresponds to rest-frame 8 μm with its strong PAH emission feature. Because of the strong emission feature and its difference from object to object, the K-correction may have large scatter. Objects in our sample are in a rather narrow redshift range, and the K-correction needed to covert 24 μm flux to the $L(8\ \mu{\rm m})$ is close to zero. We stacked all the spectra together to generate a mean rest-frame spectrum for the sample and used it to calculate the K-correction as a function of redshift. The derived 8 μm luminosities are given in Table 3 and range from $10^{11.41}$ to $10^{11.79}$ $L_\odot$.

There have been several studies of the $L(8\ \mu{\rm m})$–$L_{\rm IR}$ relation. Bavouzet et al. (2008) used an IR-selected galaxy sample at $z < 0.6$ to derive an empirical relation $L_{\rm IR} = 1.3 \times 10^{12}(L(8\ \mu{\rm m})/10^{11.5})^{0.83}$. Caputi et al. (2007) used the same sample to find $L_{\rm IR} = 3.0 \times 10^{12}(L(8\ \mu{\rm m})/10^{11.5})^{1.06}$, i.e., slightly higher $L_{\rm IR}$ for a given $L(8\ \mu{\rm m})$. The inconsistency may come from objects at $0.3 < z < 0.6$ in the sample. Huang et al. (2007) showed that the 7.7 μm PAH feature begins to shift out of the IRAC 8 μm band for $z > 0.3$. The K-correction to calculate $L(8\ \mu{\rm m})$ for galaxies in $0.3 < z < 0.6$ from their 8 μm flux densities is strongly model dependent and may introduce a large uncertainty in the resulting $L(8\ \mu{\rm m})$. On the other hand, the $L(8\ \mu{\rm m})$–$L_{\rm IR}$ relation at different redshifts may differ because IR samples select different populations at different redshifts. Sajina et al. (2008) performed MIPS 70 and 160 μm and ground-based millimeter imaging of $z \sim 2$ ULIRGs and measured $L_{\rm IR}$ directly from the FIR and millimeter photometry. Their $L(8\ \mu{\rm m})$–$L_{\rm IR}$ relation is consistent with that of Bavouzet et al. (2008). Huang et al. (2009) performed FIR and millimeter photometry for their ULIRG sample and obtained a different $L(8\ \mu{\rm m})$–$L_{\rm IR}$ relation as shown in Figure 6. This relation was recently confirmed by Magdis et al. (2010) with *Herschel*/PACS and SPIRE imaging at 100, 160, 250, 350, and 500 μm. Figure 6 shows that, for a given $L(8\ \mu{\rm m})$, FIR-selected galaxies (Caputi et al. 2007; Bavouzet et al. 2008) appear to have higher $L_{\rm IR}$ than galaxies selected by UV–visible color (Reddy et al. 2006), though this may be confounded by the differing sample redshifts. Figure 6 also shows that the samples of both Huang et al. (2009) and Magdis et al. (2010) have an $L(8\ \mu{\rm m})$–$L_{\rm IR}$ relation consistent with that of Caputi et al. (2007). The galaxies in our sample have lower $L(8\ \mu{\rm m})$ than those of Huang et al. (2009) and Magdis et al. (2010), and their $L(8\ \mu{\rm m})$–$L_{\rm IR}$ relation

is unknown. We have used the Caputi et al. (2007) relation to calculate $L_{\rm IR}$, but the results are yet to be confirmed with *Herschel*/SPIRE photometry. Table 3 includes $L_{\rm IR}$ calculated with both the Caputi et al. and the Bavouzet et al. (2008) relations for comparison. All sources in the sample have $L_{\rm IR} > 10^{12}$ $L_\odot$ no matter which relation is used. Table 3 also shows the derived SFR using the Kennicutt (1998) relation[4] applied to the Caputi et al. $L_{\rm IR}$. The median SFR for ULIRGs in our sample is 570 $M_\odot$ yr^{-1} (250 $M_\odot$ yr^{-1} with the Bavouzet et al. relation).

4.2. Stellar Population and Mass in ULIRGs

Stellar population modeling (e.g., Bruzual & Charlot et al. 2003) provides a way to determine stellar parameters from observed photometry. ULIRGs have a bursty star formation history, very young stellar populations, and non-uniform dust distribution, all of which introduce large uncertainties in modeling their stellar populations. Despite those concerns, stellar masses deduced from rest NIR data are the most robust property against variations in star formation history, metallicities, and the extinction law (Förster Schreiber et al. 2004). In deriving stellar masses, we assumed constant SFR, which should be a good approximation given that the ULIRGs are observed to be undergoing intensive star formation. Several groups have demonstrated that a constant SFR provides a reasonable description of stellar population evolution for galaxies with ongoing star formation at high redshifts, such as LBGs, Lyman-alpha emitters (LAEs), star-forming BzKs, and DRGs (Shapley et al. 2001; van Dokkum et al. 2004; Rigopoulou et al. 2006; Kong et al. 2006; Lai et al. 2007). With very young stellar populations, stars on the asymptotic giant branch (AGB) make a significant contribution to the galaxy NIR emission (Maraston 2005). The initial mass function (IMF) is also in question; Daddi et al. (2007) argued that the Kroupa IMF fits ULIRGs beter than other choices. For the present work, we fit the observed SED of each source using updated Bruzual & Charlot et al. (2003) models (S. Charlot 2006 private communication, but widely known as CB07) with a Kroupa IMF and a constant star formation rate. Figure 7 shows the observed photometry, best-fit models, and inferred stellar masses for the 14 ULIRGs in our sample. The stellar masses are in the range $10.9 < \log(M_*/M_\odot) < 11.7$.

Star-forming galaxies in the local universe follow a tight correlation between stellar mass and SFR, defining a main sequence (MS) (Brinchmann et al. 2004; Peng et al. 2010). The MS is also seen at $0.5 < z < 3$ (Noeske et al. 2007; Elbaz et al. 2007; Daddi et al. 2007; Rodighiero et al. 2011). Figure 8 shows SFR versus stellar mass for our sample. As shown,

[4] $\mathrm{SFR}\,(M_\odot\ \mathrm{yr}^{-1}) = 4.5 \times 10^{-44} L_{\rm IR}\ (\mathrm{erg\,s}^{-1})$

almost all of the most massive ULIRGs follow the MS, implying that these ULIRGs share similar stellar population properties, while the five least-massive ULIRGs lie above the MS. The four X-ray sources lie at the MS (see Figure 8).

4.3. Morphologies of ULIRGs

Morphologies of ULIRGs in this sample provide direct information on how these objects formed and how their intensive star formation was triggered. It is very challenging to study morphologies of dusty galaxies at high redshifts. Observed visible light probes the rest-frame UV bands for objects at $z \sim 2$, and therefore their apparent morphologies can easily be changed by patchy dust extinction. For example, a disk galaxy at $z \sim 2$ with a patchy dust distribution may look like an irregular galaxy in the visible bands. Recent deep *HST* visible imaging shows that most distant galaxies have apparent irregular morphologies (Abraham et al. 1996; Abraham & van den Bergh 2001; Lotz et al. 2006), and Huang et al. (2009) showed that IRAC-selected ULIRGs have irregular, clumpy morphologies in the *HST*/ACS F814W band.

The *HST*/ACS visible imaging covers the central half of the EGS, and only a fraction of our IRAC-selected ULIRGs are in the ACS imaging area. Figure 9 shows ACS I-band (F814W) stamp images for 14 ULIRGs, five from the present sample and nine from Huang et al. (2007). All of them show either extended, irregular morphologies or no detection However, these rest-UV images view only the hottest stars and can be heavily affected by dust extinction, and it is therefore essential to study morphologies in the rest-frame visible, which shifts to the observed NIR. CANDELS is the largest *HST* F125W and F160W imaging survey with the newly installed NIR camera WFC3. Its high angular resolution permits studying galaxy morphologies even at high redshifts (Grogin et al. 2011; Koekemoer et al. 2011). The EGS is one of five fields in CANDELS. Only a part of CANDELS EGS imaging is available now, and so far only four objects in our sample (EGS11/EGS25/EGS27/EGS34) are detected at F125W and F160W. Figure 10 compares their visible and NIR morphologies. All four objects are very red and barely detected in the F814W band, but their NIR morphologies differ from each other. To describe clearly the morphologies of these sources, we have performed nonparametric measures of galaxy morphology in the H-band images, such as Gini coefficient (the relative distribution of the galaxy pixel flux values, or G) and M_{20} (the second-order moment of the brightest 20% of the galaxy's flux) (Lotz et al. 2006). As shown in the $H-$band panels of Figure 10, our results are consistent with the $G = 0.4M_{20}+0.9$ relation defined by Bussmann et al. (2011): Galaxies with $G < 0.4M_{20}+0.9$ have diffuse structures or multiple bright nuclei in appearance (EGS11 and EGS27). Objects

with $G > 0.4M_{20}+0.9$, they are relatively smooth with a single nucleus (EGS25 and EGS34).

EGS11 is an IRAC-selected source from Huang et al. (2009). It is detected in both ACS F606W and F814W though faintly, and its visible morphology is hard to discern but consistent with being point-like. The NIR morphology in contrast shows a clumpy, irregular pattern in an overall linear structure. This type of morphology was first discovered in early *HST* imaging of distant galaxies and thought to indicate galaxies undergoing intensive star formation (Cowie et al. 1994).
EGS25 shows a disk or possibly spiral morphology with a prominent central bulge. This source is an X-ray sources and identified by its MIPS 24 μm and 1.4 GHz radio emission to harbor an AGN (discussed in Sec. 4.4). This source is a ULIRG with AGN yet has an early-type spiral morphology. Usually such a disk galaxy cannot survive a major merger (Di Matteo et al. 2005). On the other hand, this galaxy has a SFR as high as 640 $M_\odot$ yr^{-1} compared to just a few tens of $M_\odot$ yr^{-1} at most in the disks of local spiral galaxy (Kennicutt 1998). We speculate that the circumnuclear region is forming stars through fast collapse (Granato et al. 2004; Lapi et al. 2011) while keeping or growing the disk at the same time (perhaps through accretion of high-angular-momentum gas).
EGS27 is not detected at F606W and F814W, qualifying it as a DOG (Dey et al. 2008). Its NIR morphology is very extended and clumpy. This source is also an X-ray source, but it has no point-like structure detected at either F125W or F160W. This suggests obscuration, but the MIR spectrum (Fig. 4) does not exhibit especially strong silicate absorption.
EGS34 shows two distinctively different components within 1.″0: one point component and one extended, low-surface-brightness component. This source is also an X-ray source. The point source is detected at ACS F606W and F814W, but the extended component is very red and is not detected at these wavelengths. The X-ray emission is likely from the point source. The two components could be a projection of two objects at different redshifts with the extended source contributing little or no MIPS 24 μm emission.

4.4. AGN in ULIRGs

One of the surest ways of identifying an AGN is to measure its X-ray luminosity. Four objects in our sample, EGS22/EGS25/EGS27/EGS34, are X-ray sources in the Chandra 800 ks AEGIS-X catalog (Nandra et al. 2007; Laird et al. 2009). Only one (EGS22) of the four X-ray-selected ULIRGs has $[3.6]-[4.5] > 0$ and $[5.8]-[8.0] < 0$. Their X-ray fluxes $F(0.5-10$ keV) are 7.7×10^{-16}, 1.7×10^{-15}, 1.7×10^{-15}, and 5.7×10^{-16} erg cm^{-2} s^{-1}, respectively, corresponding to X-ray luminosities $L_{\rm X}$ of 1.7×10^{43}, 2.5×10^{43}, 5.6×10^{43}, and

1.0×10^{43} erg s^{-1}. Intensive star formation in ULIRGs, however, can also generate such a high X-ray luminosity (Laird et al. 2010). Figure 11 compares X-ray luminosity and inferred $L_{\rm IR}$. EGS22 and EGS34 have $L(2-10\ {\rm keV})/L_{\rm IR}$ ratios consistent with the $L(2-10\ {\rm keV})$–SFR conversion ratio proposed by Ranalli et al. (2003), while $L(2-10\ {\rm keV})/L_{\rm IR}$ for EGS25 and EGS27 are higher and indicate an AGN contribution. Only EGS27 has a low X-ray hardness ratio of -0.29. Thus it is a Type 1 (unobscured) AGN based on its X-ray luminosity and hardness ratio (Messias et al. 2010). The remaining 10 ULIRGs in the sample are not detected in X-rays with upper limit $L_X < 1.3\times10^{42}$ erg s^{-1} and thus show no indication of an AGN. However, an AGN could still be present if it is weak or the X-rays are obscured.

Radio 1.4 GHz emission can also be used to identify AGNs. Starburst-dominated IR-luminous galaxies have a typical $L_{\rm IR}: L_{1.4\ {\rm GHz}}$ ratios characterized by $q = 2.35$[5] (Yun et al. 2001), while AGNs have much lower q because the active nuclei emit non-thermal synchrotron radio radiation but relatively little FIR radiation. The bright IRAC-selected galaxies in the EGS (Huang et al. 2009) have $q \sim 2.15$, slightly lower than $q = 2.35$ (see Figure 12). Power-law ULIRGs have much lower q in the range of $1.6 < q < 2.15$ (Sajina et al. 2008; Huang et al. 2009), indicating a much higher AGN fraction. Kovács et al. (2006) measured $L_{\rm IR}$ using 350 μm, 850 μm, and 1.2 mm flux densities and obtained a mean $q = 2.07\pm0.3$ for SMGs at $1 < z < 3$. Four galaxies in our sample, EGS6/EGS9/EGS25/EGS34, are detected in the 1.4 GHz radio catalog (Ivison et al. 2007). They have $q = 2.36$, 1.66, 2.10, and 2.05, respectively. Thus only EGS9 shows a strong radio excess. Even EGS25, an X-ray AGN, has relatively large $q = 2.10$. The remaining 10 ULIRGs in the sample were not detected at 1.4 GHz with radio upper limits corresponding to $q \gtrsim 2.12$.

Hot dust emission in the rest 3 $\mu{\rm m} < \lambda < 8$ μm wavelength range is another sign of an AGN (Carleton et al. 1987; Shi et al. 2005, 2007). The IRAC 8 μm and AKARI 15 μm photometric data correspond to rest-frame 2.7 and 4.5 μm, respectively. The AKARI 15 μm photometry is rather shallow, and only the three X-ray-selected sources (EGS25/EGS27/EGS34) were detected. Their luminosities $L(4.5\ \mu{\rm m\ rest})$ are 7.8×10^{10}, 4.9×10^{10}, and 4.3×10^{10} L$_\odot$ respectively. These values are comparable to the X-ray luminosities with $L_X/L(4.5\ \mu{\rm m}) = 0.08$, 0.30, and 0.06, consistent with AGN SEDs (e.g., Elvis et al. 1994). These galaxies also show red $[5.8]-[8.0]$ colors, consistent with a steeply-rising AGN continuum. EGS25 has the highest 15 μm emission in the sample; its $F(15\ \mu{\rm m})/F(24\ \mu{\rm m})$ ratio is consistent with the ratio for a QSO at the same redshift (Huang et al. 2009).

The observed $[4.5]-[8.0]$ color characterizes the ratio of stellar emission (rest 1.5 μm at $z = 2$) to hot dust emission. Figure 13 shows that seven of nine ULIRGs Weedman et al.

[5] $q \equiv \log(F_{\rm FIR}/3.75\times10^{12}\ {\rm W\ m^{-2}}) - \log(F_{1.4\ {\rm GHz}}/{\rm W\ m^{-2}\ Hz^{-1}})$ defined by Condon (1992).

(2006) identified as powered primarily by AGNs have $[4.5]-[8.0] \gtrsim 0.75$, the criterion proposed by Pope et al. (2008) to separate AGN- from starburst-dominated SMGs. The Weedman et al. (2006) AGNs also have $[8.0]-[24] \lesssim 2.5$. In contrast, all the IRAC-selected ULIRGs (Weedman et al. 2006; Farrah et al. 2008; Huang et al. 2009; Desai et al. 2009) have $[4.5]-[8.0] < 0.75$, and most have $[8.0]-[24] > 2.5$. All objects in our sample except the ones detected in X-rays have these colors, but those detected in X-rays have $[8.0]-[24] \lesssim 2.5$ colors but still $[4.5]-[8.0] < 0.75$. These colors may indicate a mix of processes in which objects have both intensive star formation and AGNs.

5. Summary

Applying two IRAC color criteria (inequality 1) to objects with $0.2 < F(24\ \mu\mathrm{m}) < 0.6$ mJy produces a sample of ULIRGs that are star-forming, not AGN-dominated. The 14 sources fall into a narrow redshift range around $z \sim 1.95 \pm 0.19$ and have PAH features at 7.7, 8.6, and 11.3 μm. The redshift distribution in our sample is very similar to that of all SB-dominated ULIRGs ($z \sim 2$) selected at 24 μm. The objects have stellar masses of $M_* > 10^{11}$ $\mathrm{M}_\odot$, similar to stellar masses of DRGs, BzKs, and SMGs. Indicated SFRs, based on rest-frame 8 μm luminosities and the Caputi et al. (2007) $L(8\ \mu\mathrm{m})$–L_{IR} relation, are in the range of 410 to 1100 $\mathrm{M}_\odot\ \mathrm{yr}^{-1}$.

Four objects in the sample are detected in X-rays (three having been initially selected as X-ray sources), but the X-ray luminosities for two of them can be accounted for by their intensive star formation. The remaining two objects have higher $L_{2-10\ \mathrm{keV}}$ than their star formation can produce, indicating that they harbor AGNs. MIR colors of all 14 sources in the sample are consistent with starbursts, but three of the X-ray sources have high 4.5 μm luminosities, relatively red $[4.5]-[8.0]$ colors, and relatively blue $[8.0]-[24]$ colors, consistent with an AGN contribution to the emission. FIR/radio ratios for this sample are consistent with $q = 2.35$ without showing strong radio excess from AGN except for one source (EGS9, not one of the X-ray sources) which has $q = 1.66$. Ten of 14 objects in the sample show no indication that an AGN is present, and in no object does an AGN appear to dominate the luminosity.

Only four objects in the sample have so far been studied with *HST*/WFC3 F160W imaging. Their rest-frame visible morphologies are diverse with one apparent early-type spiral and the others irregular but of differing descriptions. This diversity suggests that there may be multiple formation process for ULIRGs, but a larger sample of imaging is needed (and is now in progress in the CANDELS program) to reach any strong conclusions. The observed visible *HST*/ACS imaging probes the rest-frame UV for this sample. Some

objects in the sample are so red that they are barely detected at F814W. Those that are seen show irregular and clumpy morphologies, consistent with star formation heavily obscured by patchy dust.

We are grateful to the referee for the comments which have improved this paper greatly. We thank Robert G. Abraham, Christopher J. Conselice and Yu Dai for their valuable suggestions. This work is based on observations taken by the CANDELS Multi-Cycle Treasury Program with the NASA/ESA *HST*, which is operated by the Association of Universities for Research in Astronomy, Inc; under NASA contract NAS5-26555. This work is based in part on observations made with the *Spitzer Space Telescope*, which is operated by the Jet Propulsion Laboratory, California Institute of Technology under a contract with NASA. Support for this work was provided by NASA through an award issued by JPL/Caltech. This work was also supported by the National Natural Science Foundation of China (NSFC, No. 11225315), the Chinese Universities Scientific Fund (CUSF), and the Specialized Research Fund for the Doctoral Program of Higher Education (SRFDP, No. 20123402110037).

REFERENCES

Abraham, R. G., Tanvir, N. R., Santiago, B. X., et al. 1996, MNRAS, 279, L47

Abraham, R. G., & van den Bergh, S. 2001, Science, 293, 1273

Arnouts, S., Walcher, C. J., Le Fvre, O., et al. 2007, A&A, 476, 137

Barmby, P., Huang, J.-S., Ashby, M. L. N., Eisenhardt, P. R. M., Fazio, G. G., Willner, S. P., & Wright, E. L. 2008, ApJS, 177, 431

Bavouzet, N., Dole, H., Le Floc'h, E., et al. 2008, A&A, 479, 83

Bell, E. F., & de Jong, R. S. 2001, ApJ, 550, 212

Brinchmann, J., Charlot, S., White, S. D. M., et al. 2004, MNRAS, 351, 1151

Bruzual, G. & Charlot, S. 2003, MNRAS, 344, 1000

Bussmann, R. S., Dey, A., Lotz, J., et al. 2009, ApJ, 693, 750

Bussmann, R. S., Dey, A., Lotz, J., et al. 2011, ApJ, 733, 21

Caputi, K. I., Lagache, G., Yan, L., et al. 2007, ApJ, 660, 97

Carleton, N. P., Elvis, M., Fabbiano, G., Willner, S. P., Lawrence, A., & Ward, M. 1987, ApJ, 318, 595

Chapman, S. C., Blain, A. W., Ivison, R. J., Smail, I. R. 2003, Nature, 422, 695

Chary, R., & Elbaz, D. 2001, ApJ, 556, 562

Condon, J. J. 1992, ARA&A, 30, 575

Cole, S., Lacey, C. G., Baugh, C. M., Frenk, C. S. 2000, MNRAS, 319, 168

Conselice, C. J., Bundy, K., Trujillo, I., et al. 2007, MNRAS, 381, 962

Cowie, L. L., Songaila, A., Songaila, A., et al. 1994, ApJ, 432, L83

Daddi, E., Cimatti, A., Renzini, A., et al. 2004, ApJ, 617, 746

Daddi, E., Dickinson, M., Chary, R., et al. 2005, ApJ, 631, 13

Daddi, E., Dickinson, M., Morrison, G., et al. 2007, ApJ, 670, 156

Dasyra, K. M., Yan, L., Helou, G., et al. 2008, ApJ, 680, 232

Dasyra, K. M., Yan, L., Helou, G., et al. 2009, ApJ, 701, 1123

Davé, R., Finlator, K., Oppenheimer, B. D., et al. 2010, MNRAS, 404, 1355

Davis, M., Guhathakurta, P., Konidaris, N. P., et al. 2007, ApJ, 660, L1

Desai, V., Soifer, B. T., Dey, A., et al. 2009, ApJ, 700, 1190

Dey, A., Soifer, B. T., Desai, V., et al. 2008, ApJ, 677, 943

Dickinson, M., Papovich, C., Ferguson, H. C., et al. 2003, ApJ, 587, 25

Di Matteo, T., Springel, V., & Hernquist, L. 2005, Nature, 433, 604

Dunne, L., Ivison, R. J., Maddox, S., et al. 2009, MNRAS, 394, 3

Elbaz, D., Daddi, E., Le Borgne, D., et al. 2007, A&A, 468, 33

Elvis, M., Wilkes, B. J., McDowell, J. C., et al. 1994, ApJS, 95, 1

Fadda, D., Yan, L., Lagache, G., et al. 2010, ApJ, 719, 425

Farrah, D., Lonsdale, C. J., Weedman, D. W., et al. 2008, ApJ, 677, 957

Fiolet, N., Omont, A., Lagache, G., et al. 2010, A&A, 524, 33

Fontana, A., Donnarumma, I., Vanzella, E., et al. 2003, ApJ, 594, L9

Förster Schreiber, N. M., van Dokkum, P. G., Franx, M., et al. 2004, ApJ, 616, 40

Franx, M., Labb, I., Rudnick, G., et al. 2003, ApJ, 587,79

Glazebrook, K., Abraham, R. G., McCarthy, P. J., et al. 2004, Nature, 430, 181

Granato, G. L., De Zotti, G., Silva, L., Bressan, A., & Danese, L. 2004, ApJ, 600, 580

Grogin, N. A., Kocevski, D. D., Faber, S. M., et al. 2011, ApJS, 197, 35

Higdon, S. J. U., Devost, D., Higdon, J. L., et al. 2004, PASP, 116, 975

Hou, L. G., Han, J. L., Kong, M. Z., Wu, X, B. 2011, ApJ, 732, 72

Houck, J. R., Soifer, B. T., Weedman, D., et al. 2005, ApJ, 622, L105

Huang, J.-S., Barmby, P., Fazio, G. G., et al. 2004, ApJS, 154, 44

Huang, J.-S., Rigopoulou, D., Papovich, C., et al. 2007, ApJ, 660, 69

Huang, J.-S., Faber, S. M., Daddi, E., et al. 2009, ApJ, 700, 183

Ivison, R. J., Chapman, S. C., Faber, S. M., et al. 2007, ApJ, 660, 77

Karim, A., Schinnerer, E., Martnez-Sansigre, A., et al. 2011, ApJ, 730, 61

Kartaltepe, J. S., Dickinson, M., Alexander, D. M., et al. 2012, ApJ, 757, 23

Kennicutt, R. C., Jr. 1998, ARA&A, 36, 189

Koekemoer, A. M., Faber, S. M., Ferguson, H. C., et al. 2011, ApJS, 197, 36

Kong, X., Daddi, E., Arimoto, N., et al. 2006, ApJ, 638, 72

Kormendy, J., Fisher, D. B., Cornell, M. E., Bender, R. 2009, ApJS, 182, 216

Kovcs, A., Chapman, S. C., Dowell, C. D., et al. 2006, ApJ, 650, 592

Labbé, I., Huang, J.-S., Franx, M., et al. 2005, ApJ, 624, 81

Lagache, G., Dole, H., Puget, J. L., et al. 2004, ApJS, 154, 112

Lai, K., Huang, J.-S., Fazio, G., et al. 2007, ApJ, 655, 704

Laird, E. S., Nandra, K., Georgakakis, A., et al. 2009, ApJS, 180, 102

Laird, E. S., Nandra, K., Pope, A., Scott, D. 2010, ApJ, 401, 2763

Lapi, A., González-Nuevo, J., Fan, L., et al. 2011, ApJ, 742, 24

Lotz, J. M., Madau, P., Giavalisco, M., Primack, J., & Ferguson, H. C. 2006, ApJ, 636, 592

Magdis, G. E., Elbaz, D., Hwang, H. S., et al. 2010, MNRAS, 409, 22

Maraston, C. 2005, MNRAS, 362, 799

McCarthy, P., Le Borgne, D., Crampton, D., et al. 2004, ApJ, 614, 9

Melbourne, J., Desai, V., Armus, L., et al. 2008, AJ, 136, 1110

Melbourne, J., Bussman, R. S., Brand, K., et al. 2009, AJ, 137, 4854

Messias, H., Afonso, J., Hopkins, A., et al. 2010, ApJ, 719, 790

Naab, T., & Burkert, A. 2003, ApJ, 597, 893

Nandra, K., Georgakakis, A., Willmer, C. N. A., et al. 2007, ApJ, 660, 11

Narayanan, D., Cox, T. J., Hayward, C. C., Younger, J. D., Hernquist, L. 2009, MNRAS, 400, 1919

Noeske, K. G., Weiner, B. J., Faber, S. M., et al. 2007, ApJ, 660, L43

Pannella, M., Carilli, C. L., Daddi, E., et al. 2009, ApJ, 698, 116

Papovich, C., Dole, H., Egami, E., et al. 2004, ApJS, 154, 70

Papovich, C., Moustakas, L. A., Dickinson, M., et al. 2006, ApJ, 640, 92

Papovich, C. 2008, ApJ, 676, 206

Peng, Y., Lilly, S. J., Kovac, K., et al. 2010, ApJ, 721, 193

Pope, A., Bussmann, R. S., Dey, A., et al. 2008, ApJ, 689, 127

Pozzetti, L., Bolzonella, M., Lamareille, F., et al. 2007, A&A, 474, 443

Ranalli, P., Comastri, A., Setti, G. 2003, A&A, 399, 39

Reddy, N. A., Steidel, C. C., Erb, D. K., et al. 2006, ApJ, 653, 1004

Richards, G. T., Strauss, M. A., Fan, X., et al. 2006, AJ, 131, 2766

Rigopoulou, D., Huang, J.-S., Papovich, C., et al. 2006, ApJ, 648, 81

Roche, P. F., & Aitken, D. K. 1985, MNRAS, 213, 789

Roche, P. F., Whitmore, B., Aitken, D. K., & Phillips, M. M. 1984, MNRAS, 207, 35

Rodighiero, G., Vaccari, M., Franceschini, A., et al. 2010, A&A, 515, 8

Rodighiero, G., Daddi, E., Baronchelli, I., et al. 2011, ApJ, 739, 40

Sajina, A., Yan, L., Armus, L., et al. 2007, ApJ, 664, 713

Sajina, A., Yan, L., Lutz, D., et al. 2008, ApJ, 683,659

Sanders, D. B., Soifer, B. T., Elias, J. H., et al. 1988, ApJ, 325, 74

Sanders, D., & Mirabel, I. F. 1996, ARA&A, 34, 749

Shapley, A., Steidel, C. C., Adelberger, K. L., et al. 2001, ApJ, 562, 95

Shi, Y., Rieke, G. H., Hines, D. C., et al. 2005, ApJ, 629, 88

Shi, Y., Ogle, P., Rieke, G. H., et al. 2007, ApJ, 669, 841

Sorba, R., & Sawicki, M. 2010, ApJ, 721, 1056

Steidel, C. C., Shapley, A. E., Pettini, M., et al. 2004, ApJ, 604, 534

Teplitz, H., Desai, V., Armus, L., et al. 2007, ApJ, 659, 941

van Dokkum, P. G., Franx, M., Förster S., et al. 2004, ApJ, 611, 703

Veilleux, S., Rupke, D. S. N., Kim, D., et al. 2009, ApJS, 182, 628

Weedman, D. W., Polletta, M., Lonsdale, C. J., et al. 2006, ApJ, 653, 101

Wu, Y., Helou, G., Armus, L., et al. 2010, ApJ, 723, 895

Willner, S. P., Ashby, M. L. N, Barmby, P., et al. 2012, ApJ, 756, 72

Yan, L., Sajina, A., Fadda, D., et al. 2007, ApJ, 658, 778

Yun, M. S., Reddy, N. A., & Condon, J. J. 2001, ApJ, 554, 803

Zamojski, M., Yan, L., Dasyra, K., et al. 2011, ApJ, 730, 125

This preprint was prepared with the AAS LaTeX macros v5.2.

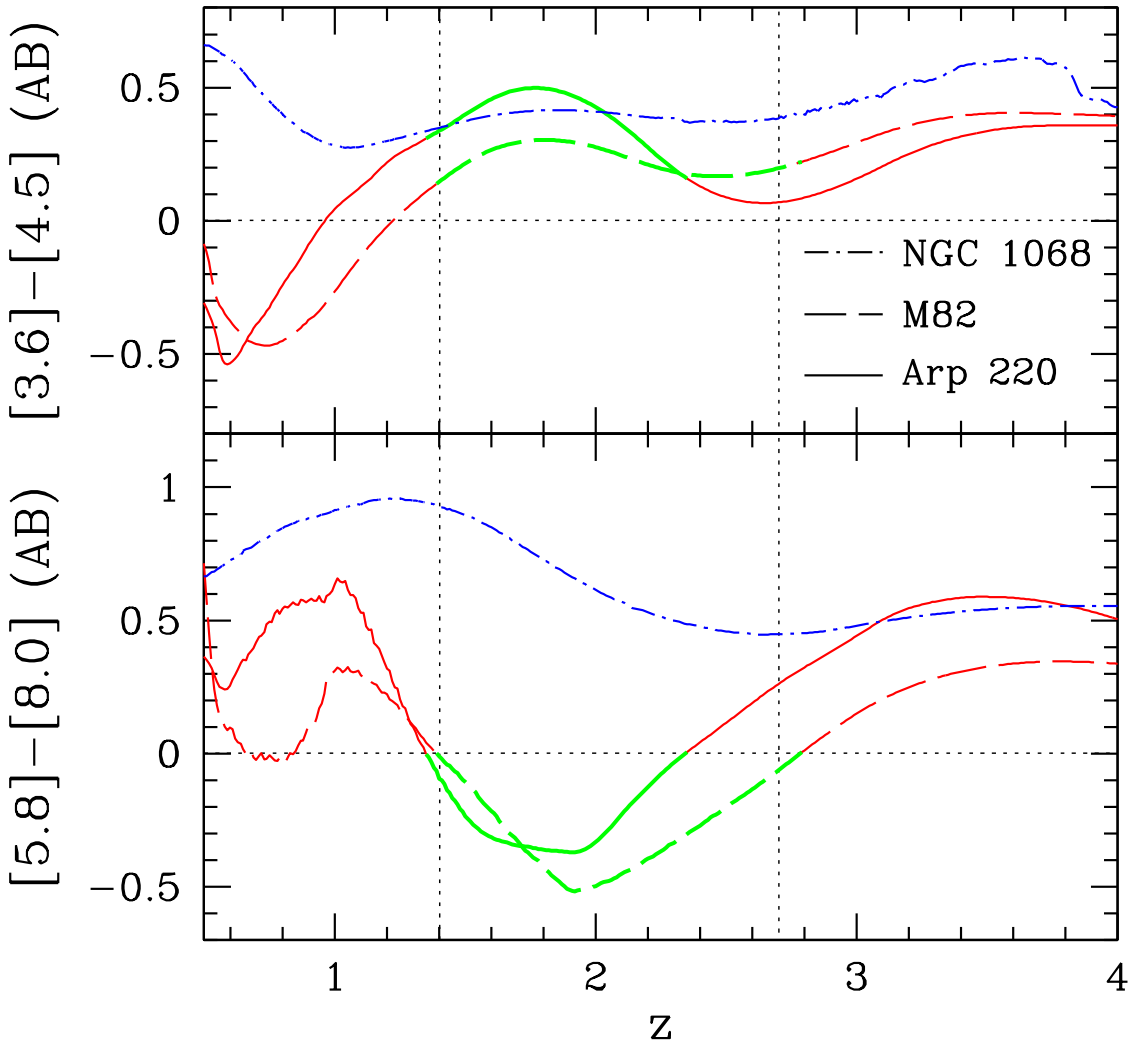

Fig. 1.— IRAC selection criteria for $z \sim 2$ ULIRGs. Lines show expected IRAC colors for three local template sources as a function of redshift. M82 (dashed lines) is a starburst, Arp 220 (solid lines) is a ULIRG, and NGC 1068 (dot-dashed lines) is an AGN. Lines are plotted in green where each template would have been selected according to the color criteria of inequality 1, which are shown as horizontal dotted lines. A galaxy with the NGC 1068 SED would not be selected at any redshift. Vertical dotted lines correspond to redshifts 1.4 and 2.7 respectively and show the approximate range of color selection.

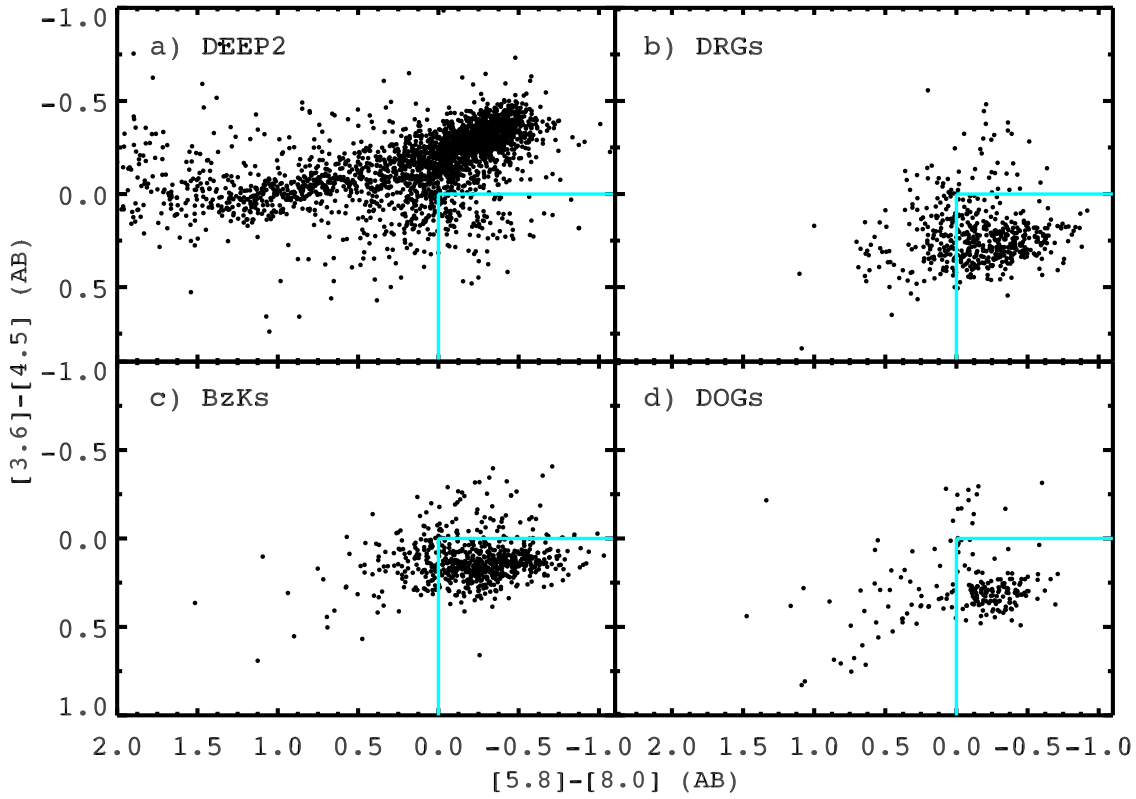

Fig. 2.— IRAC color-color diagrams for observed galaxy samples. a) AEGIS spectroscopic redshift $z < 1.4$ sample (with redshift quality Q $\geq$ 3. Q = 3: Secure redshift, Q = 4: Very secure redshift); b) Distant Red Galaxies (DRGs; Franx et al. 2003) in AEGIS; c) BzK galaxies (Daddi et al. 2004) in AEGIS; d) DOGs (Dey et al. 2008) in AEGIS. Cyan lines show the IRAC color criteria (1).

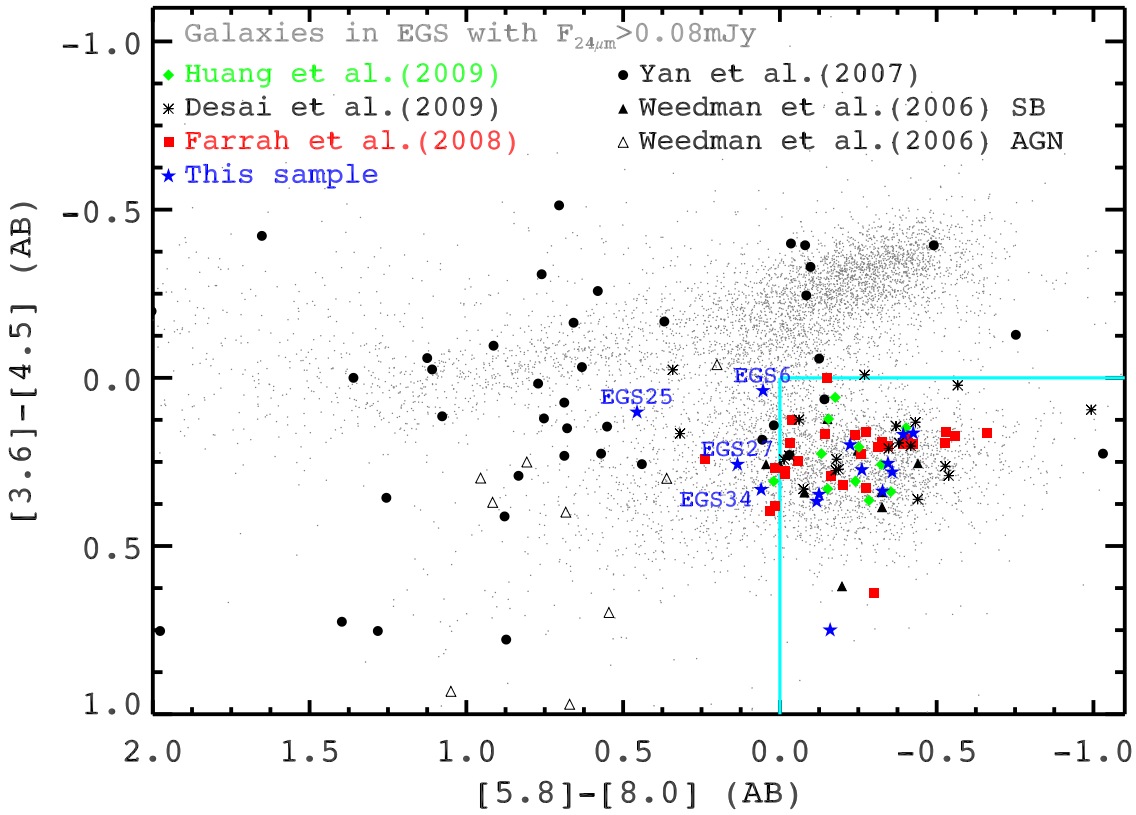

Fig. 3.— IRAC color-color diagram for EGS galaxies with $F(24\ \mu\mathrm{m}) > 0.08$ mJy. Small dots show all such galaxies; blue stars show galaxies in the current IRS spectroscopic sample, which also requires $F(24\ \mu\mathrm{m}) > 0.2$ mJy. The cyan line shows the IRAC color criteria (1). Labels indicate EGS6, which slightly misses criteria (1) because of the initial the photometry error, and three X-ray objects that are AGN candidates. Objects from other IRS spectroscopic samples (Table 2) at $z \sim 2$ are plotted for comparison, 90% of all sources in these SB-dominated samples reside in our IRAC color region (Weedman et al. 2006; Farrah et al. 2008; Desai et al. 2009; Huang et al. 2009). Yan et al. (2007) used extreme optical-to-24 μm color to select dusty sources. Sources in this sample have much redder [5.8] − [8.0] IRAC colors than the majority of 24 μm sources and are mostly AGNs as shown by their strong power-law continua, but weak or absence of PAH emission features.

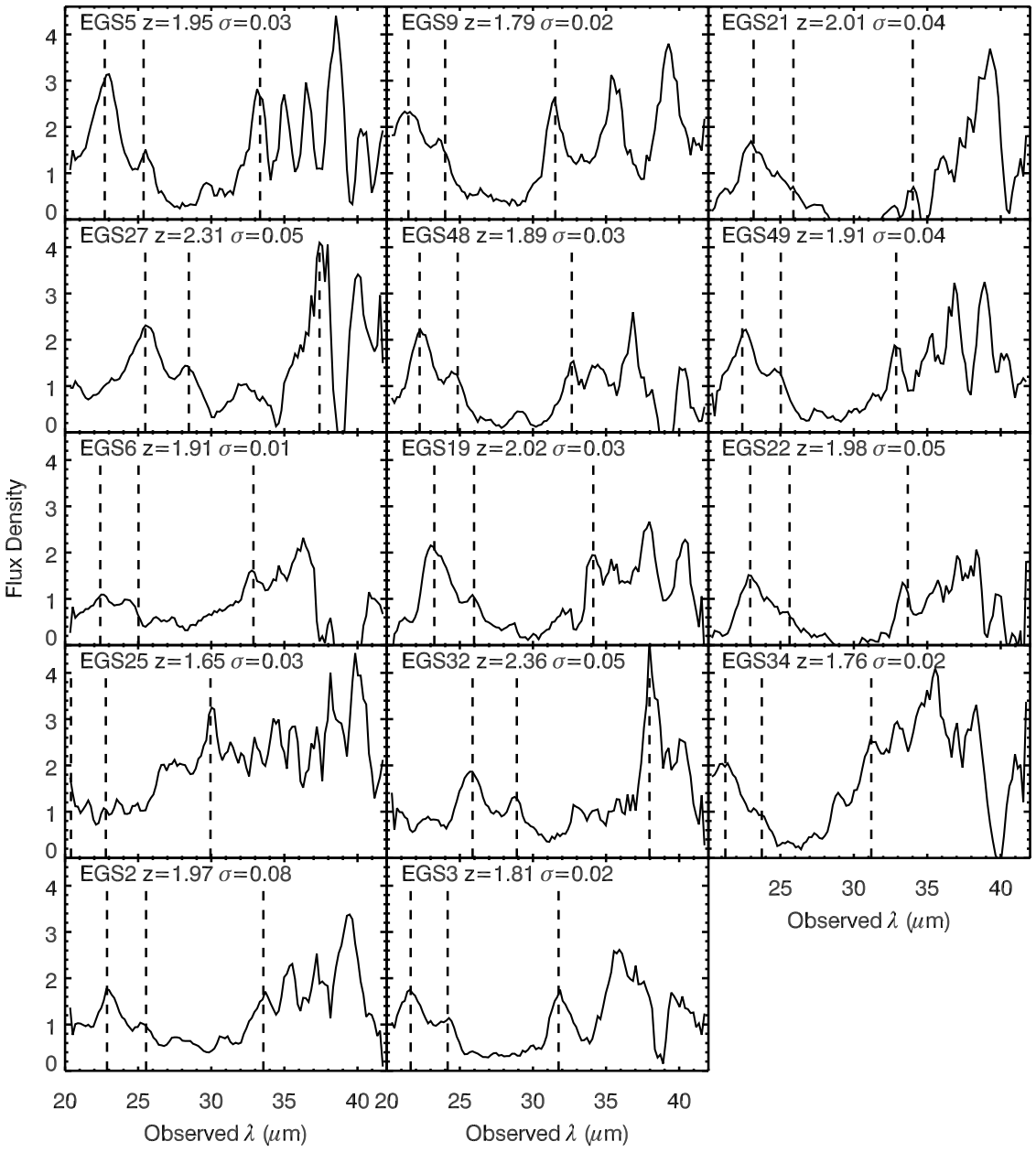

Fig. 4.— Mid-IR spectra for the 14 sources observed with IRS. The vertical scales are linear but arbitrary and different for each panel. The spectra were smoothed by a four-pixel boxcar in order to enhance the broad features such as PAH emission and silicate absorption. Dashed lines indicate the central wavelengths of the PAH emission features at rest-frame 7.7, 8.6, and 11.3 μm from left to right. The source nicknames, redshifts, and redshift uncertainties derived from the template fit are shown in each panel.

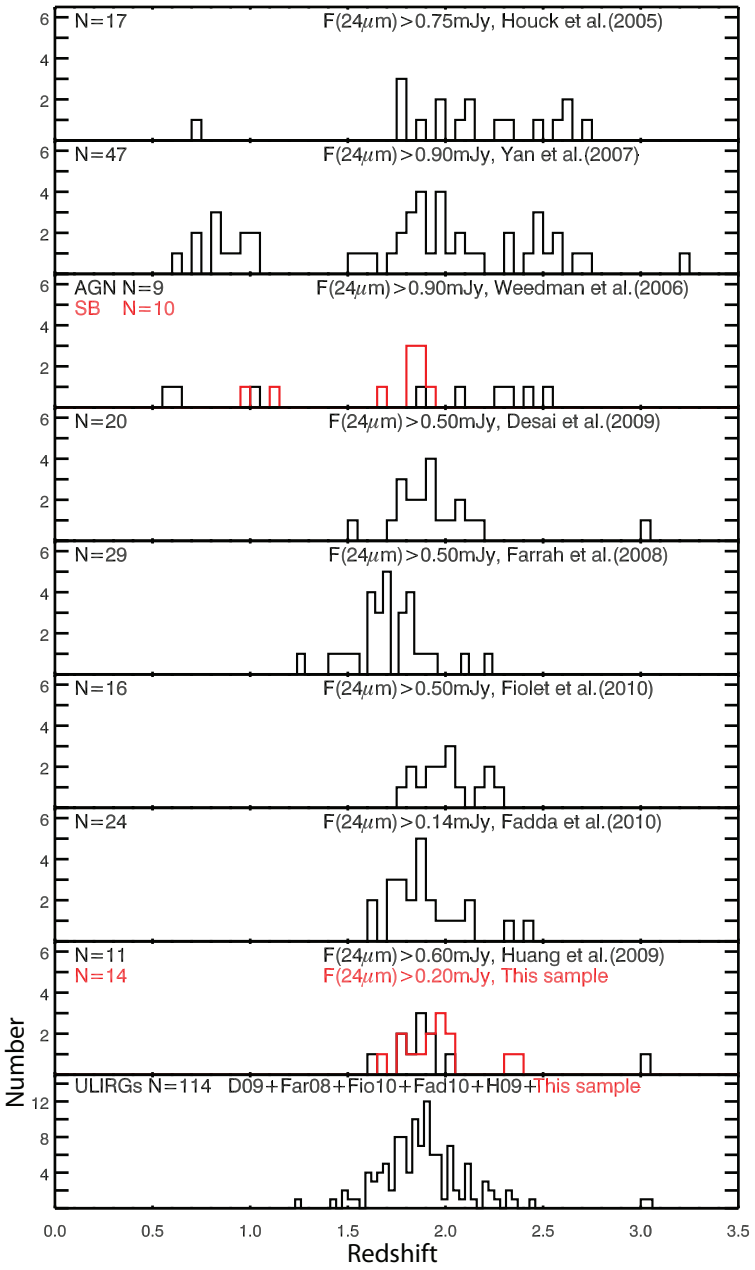

Fig. 5.— Redshift distributions for the IRS spectroscopic samples in Table 2. The number of objects in each sample and their source are indicated in each panel. AGNs and starbursts from Weedman et al. (2006) are shown separately. The bottom panel shows the redshift distribution for all 114 SB-dominated sources in the combined samples (D09+Far08+Fio10+Fad10+H09+ours, see Table 2 for detail).

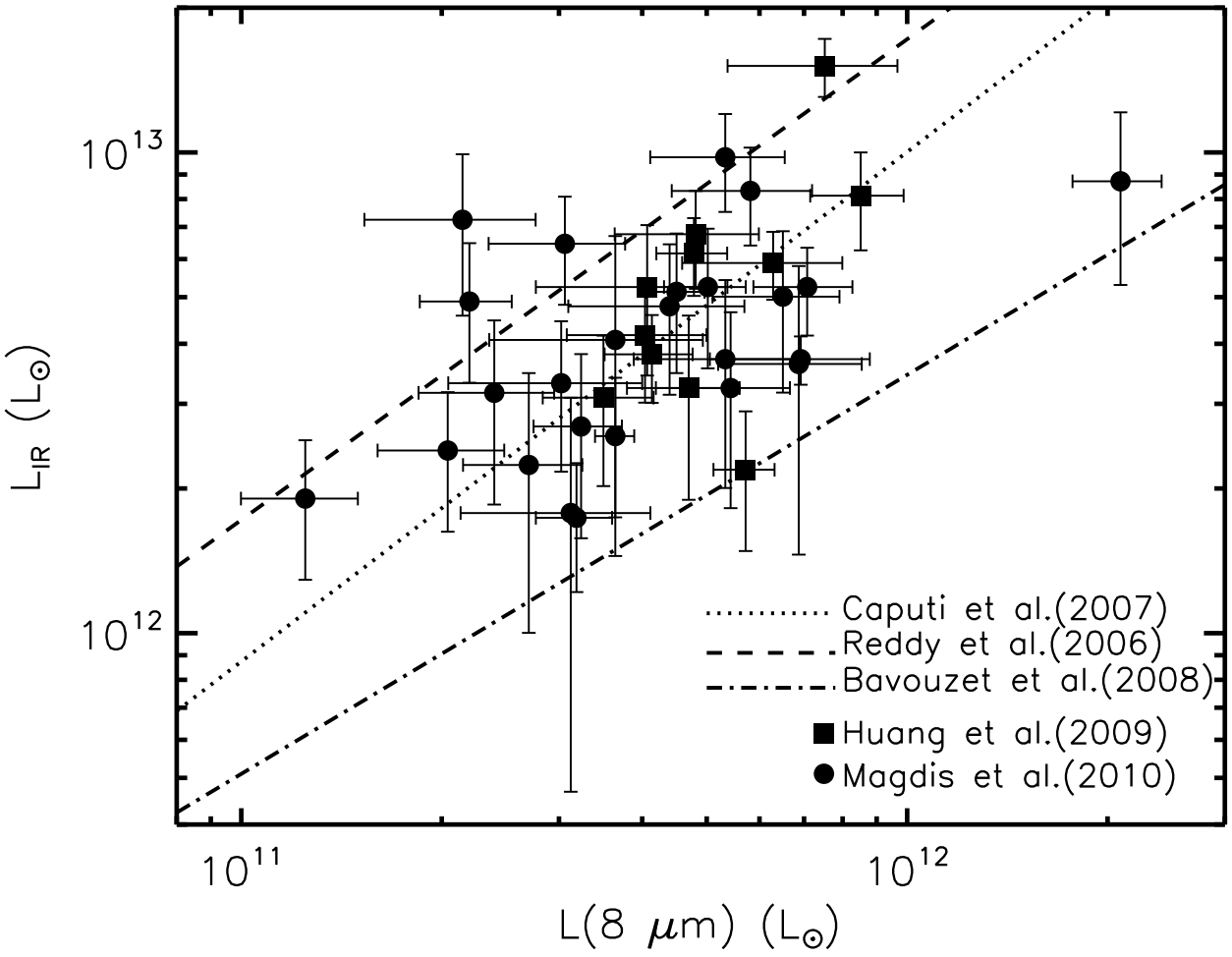

Fig. 6.— Observed IR luminosity versus rest-frame 8 μm luminosity (νL_ν) for 36 individual ULIRGs at $z \sim 2$. Filled squares denote data from Huang et al. (2009) and filled circles from Magdis et al. (2010). Lines show the local relations found by Caputi et al. (2007) (dotted) for 24 μm-selected galaxies and by Bavouzet et al. (2008) (dot-dashed) for FIR-selected galaxies. The dashed line shows the relation found by Reddy et al. (2006) for $z \sim 2$ galaxies selected by observed visible–UV colors.

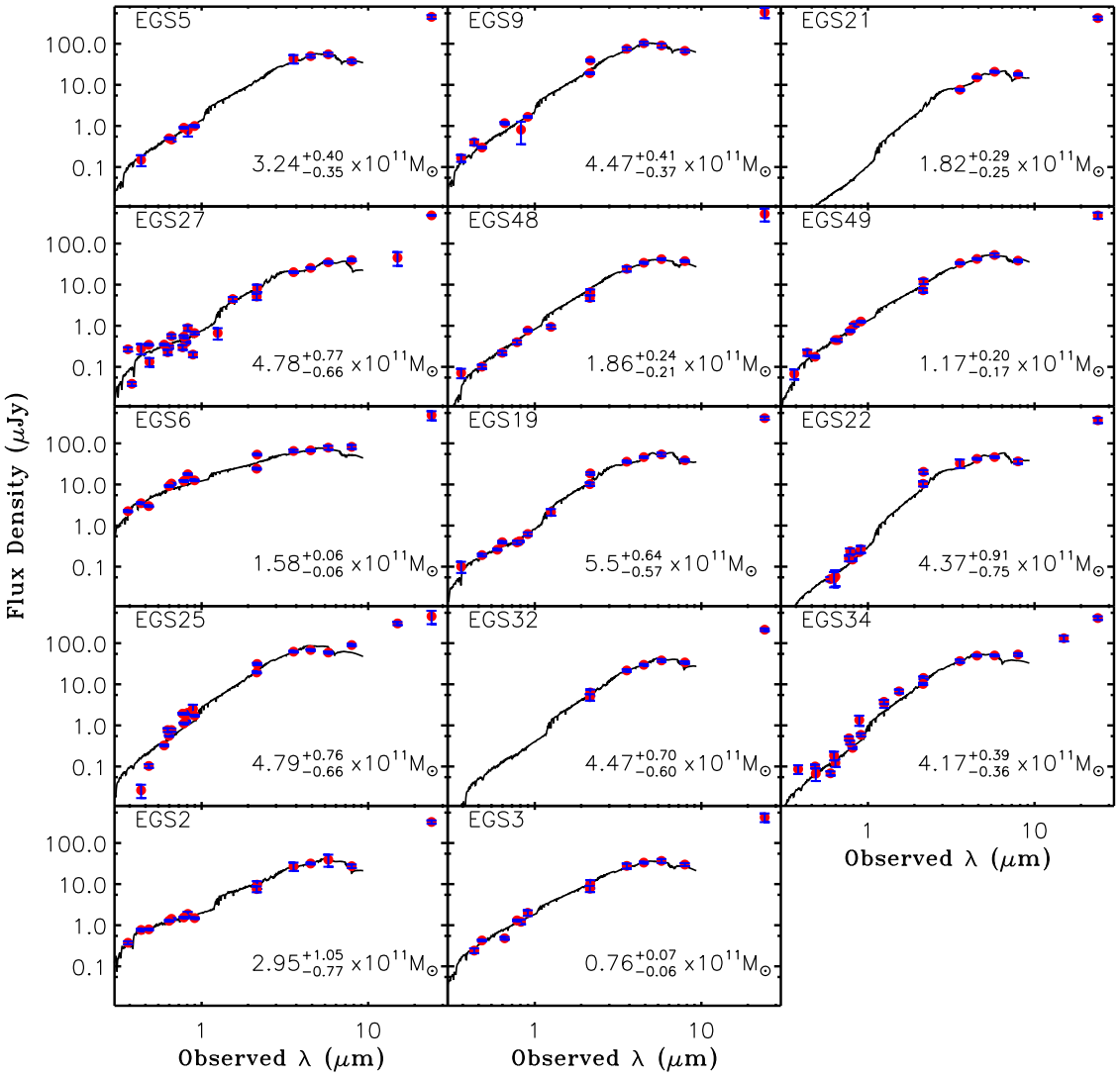

Fig. 7.— Spectral energy distributions for the 14 sample galaxies. Points show the observations, and black lines show the best-fit stellar population model (CB07). The source nickname and inferred stellar mass (M_*) are given in each panel.

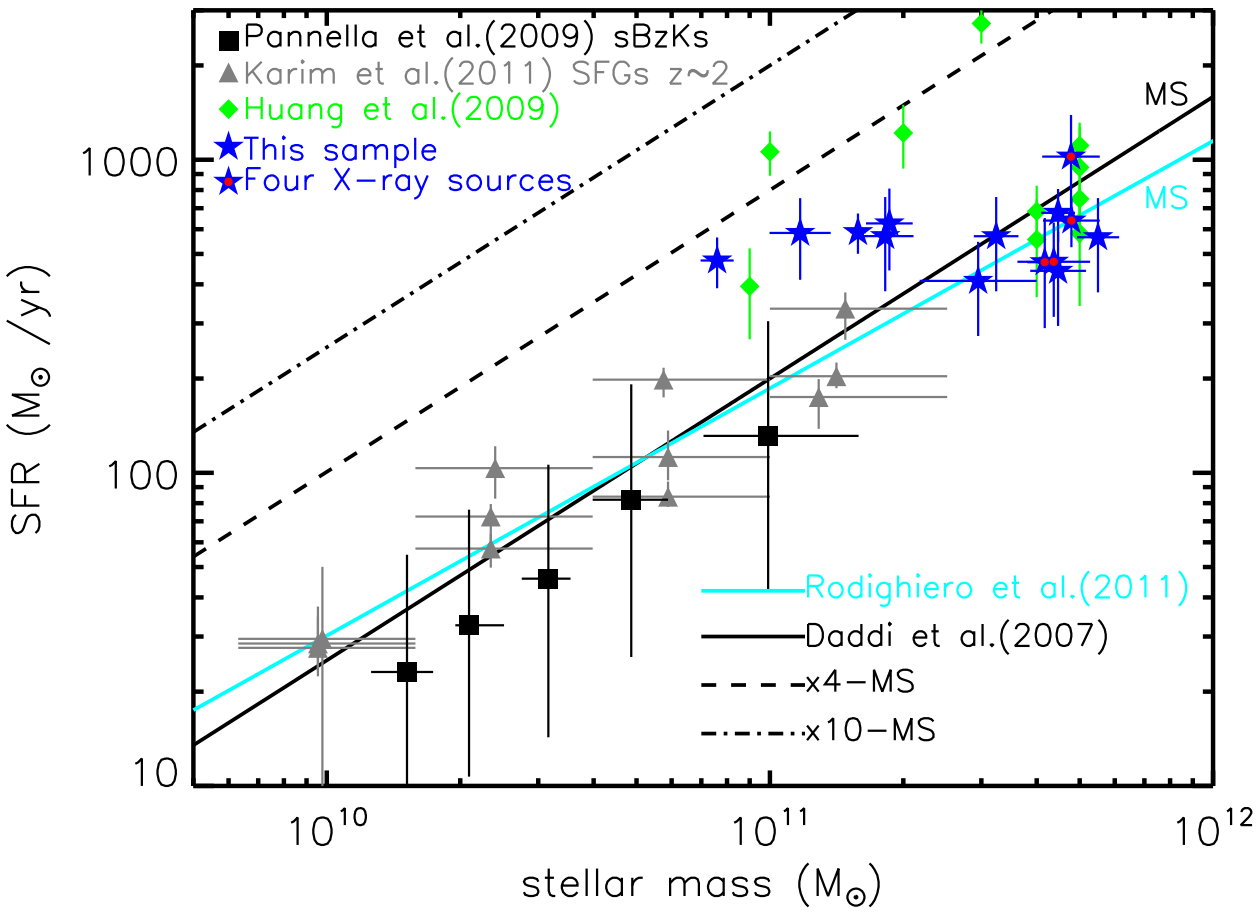

Fig. 8.— Stellar mass–SFR relation at $z \sim 2$. Blue stars denote objects in the present sample with X-ray sources indicated by superposed red dots. Filled diamonds denote individual ULIRGs from Huang et al. (2009). Filled triangles denote average SFRs for star-forming galaxies in different mass bins (Karim et al. 2011); for each mass bin, three different redshift bins from $z = 1.6$ to 3.0 are plotted. Filled squares denote average SFRs for BzK galaxies with AGNs excluded (Pannella et al. 2009). Solid black and cyan lines indicate the main sequence (MS) for star-forming galaxies at $1.5 < z < 2.5$ as defined by Daddi et al. (2007) and Rodighiero et al. (2011), respectively. Dot-dashed and dashed lines mark the loci 10 and 4 times above the Daddi et al. MS.

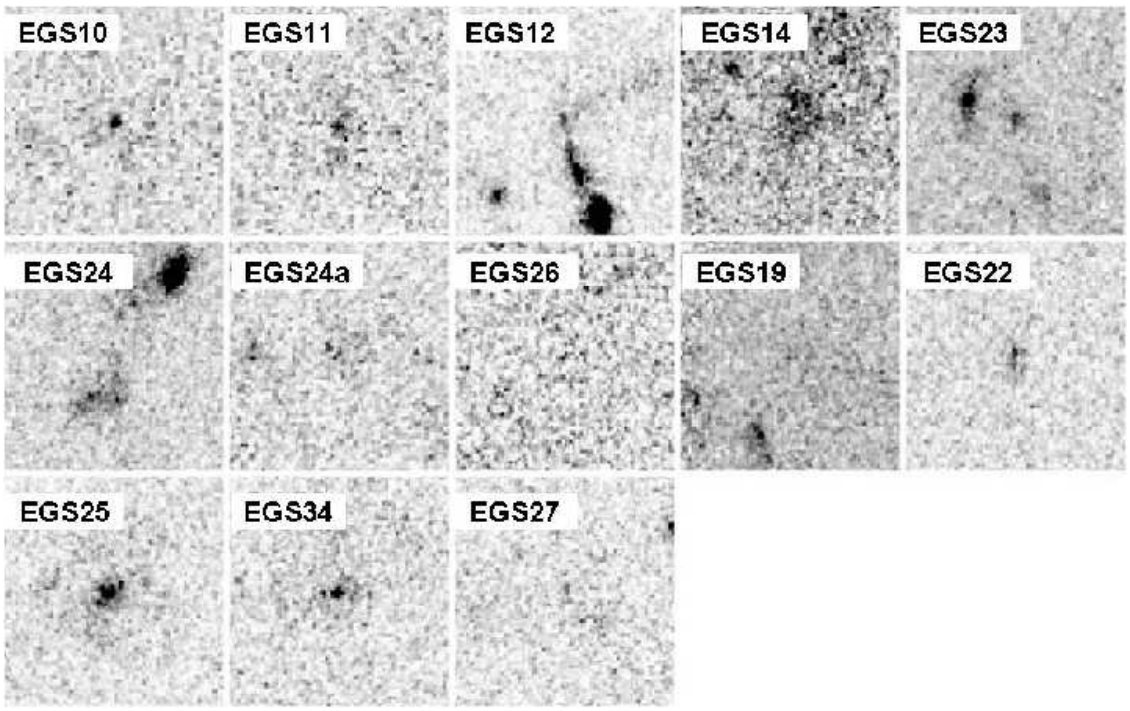

Fig. 9.— *HST*/ACS *I*-band images of 13 ULIRGs. All images are in negative grey scale and are 3″ square. Source nicknames are indicated in each panel. Five sources are from the present sample (Table 1), and the remainder are from Huang et al. (2009).

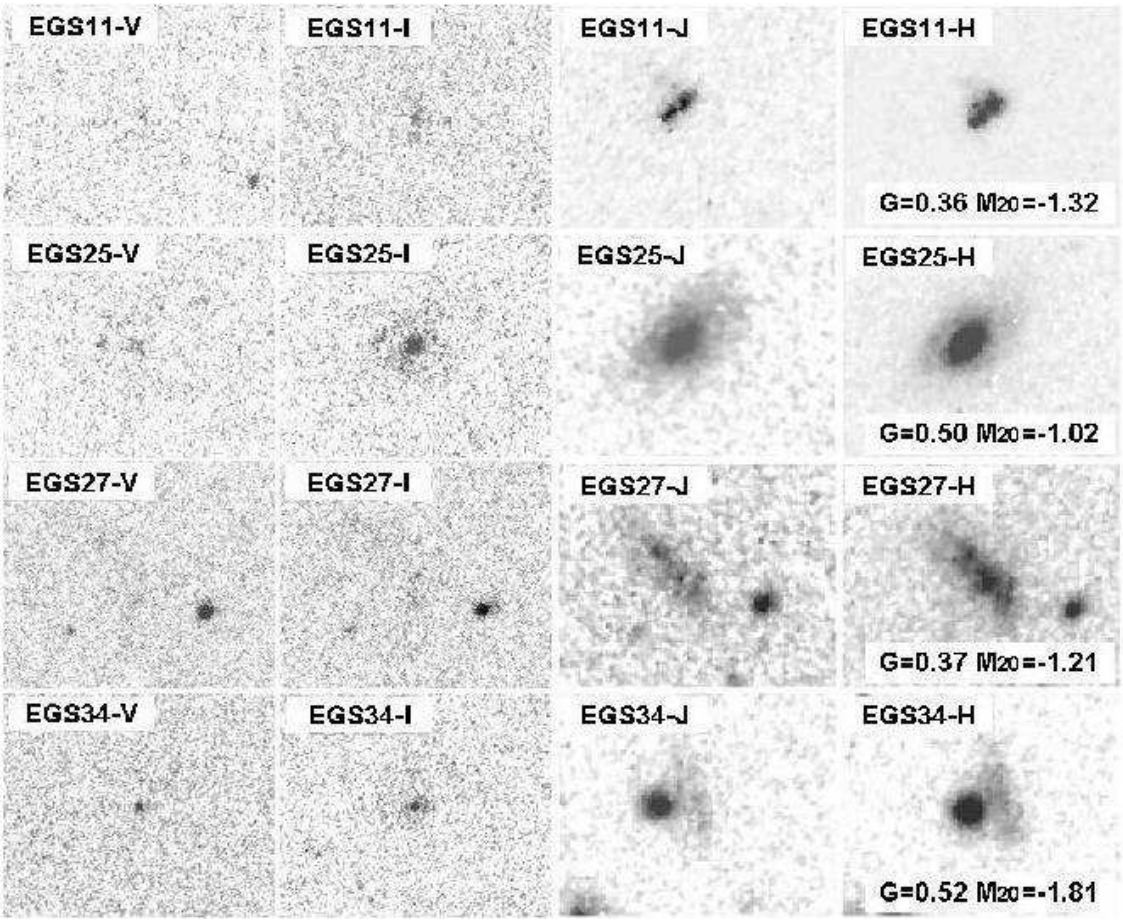

Fig. 10.— *HST*/ACS and WFC3 $V-$, $I-$, $J-$, and $H-$band images of four ULIRGs. All images are in negative grey scale and are 6″ square. Nicknames are indicated in each panel, and values of the Gini coefficient G and the M_{20} are shown in the H-band panels. The four objects shown are the only ones in the combined Huang et al. (2009) and Table 1 samples that have both ACS and WFC3 imaging.

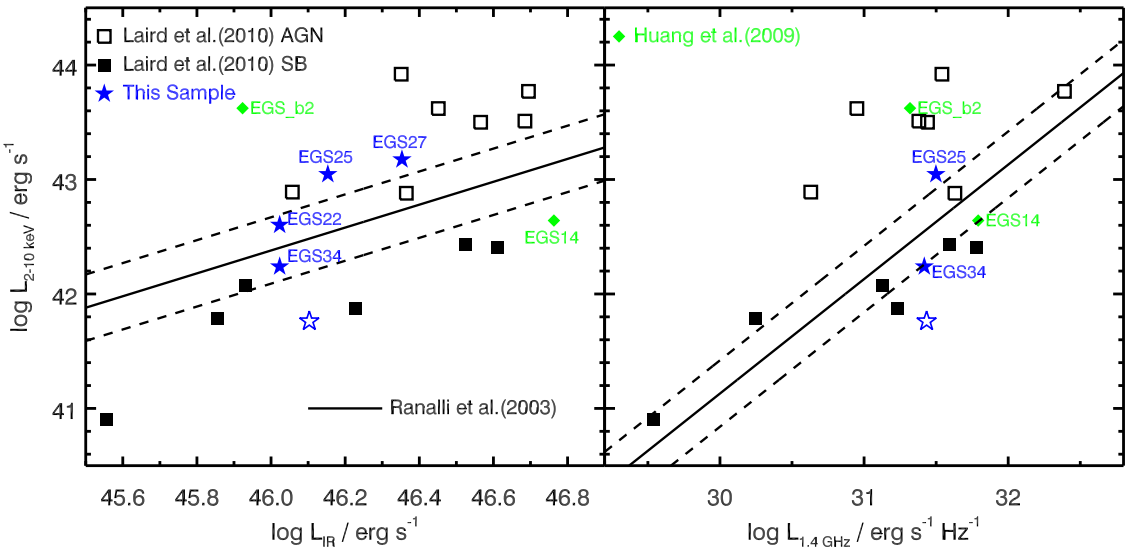

Fig. 11.— Rest-frame 2–10 keV luminosity for the X-ray-detected galaxies as functions of SFR indicators. The left panel shows $L_{\rm IR}$, and the right shows rest-frame 1.4 G̃Hz radio luminosity. Labeled stars denote individual sources from our ULIRG sample, and open stars show the stacking results for the undetected ULIRGs. EGS22/EGS27 are not in the 1.4 GHz radio catalog. Squares represent the X-ray-detected SMGs from Laird et al. (2010) with filled squares representing SMGs dominated by star formation and open squares representing AGN SMGs. Solid lines show the mean local relations for purely star forming galaxies (Ranalli et al. 2003), and dashed lines show a factor of two above and below the mean relations.

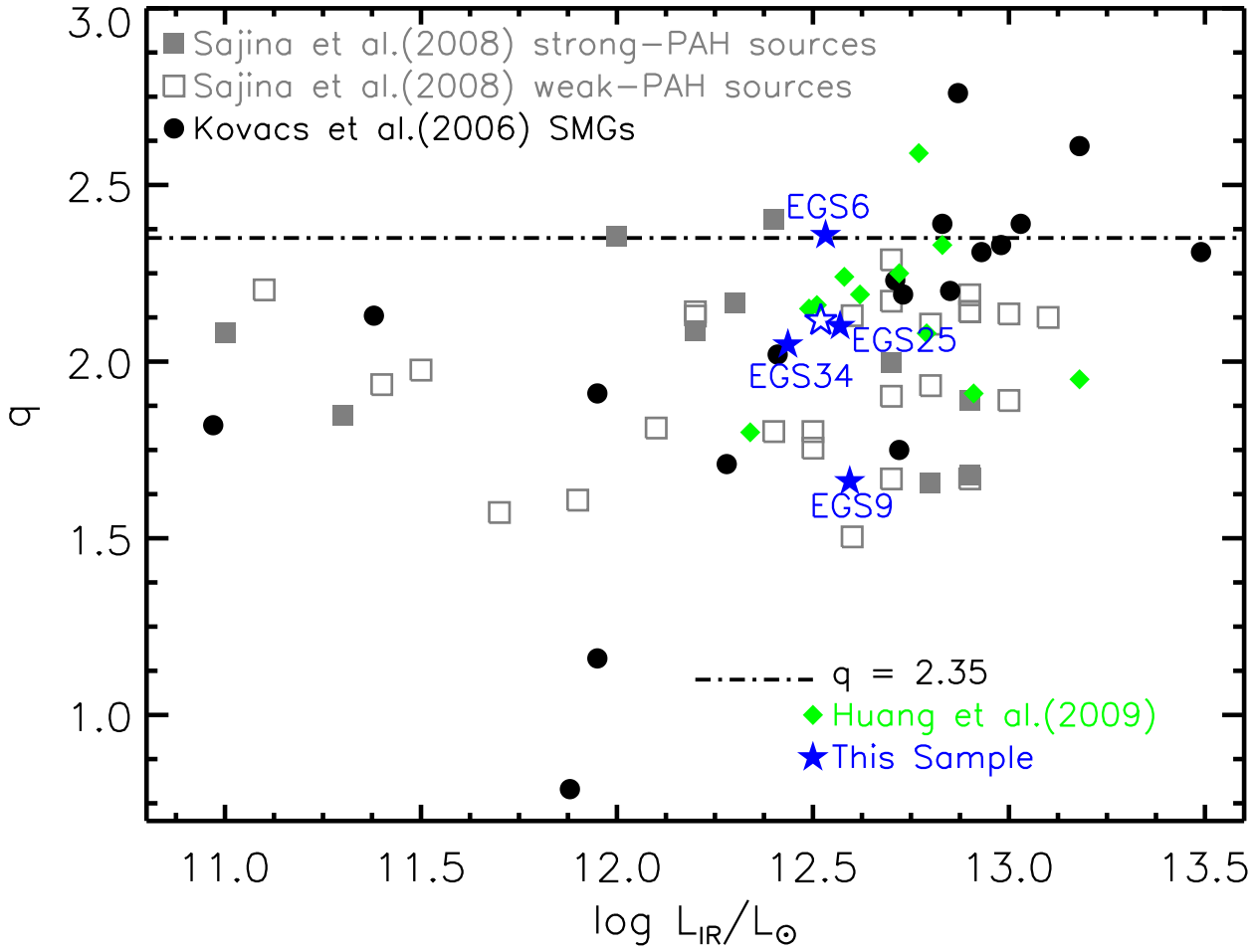

Fig. 12.— Logarithmic FIR to radio ratio as a function of $L_{\rm IR}$. The definition of q is given in Section 4.4. Labeled stars represent individual sources from our sample of ULIRGs (Table 1), and the open star shows the stacking result for the undetected ULIRGs. Other symbols show sources from three $z \sim 2$ samples (Kovács et al. 2006; Sajina et al. 2008; Huang et al. 2009) plotted for comparison. The dot-dash line indicates $q = 2.35$ (Yun et al. 2001), typical of starburst-dominated ULIRGs.

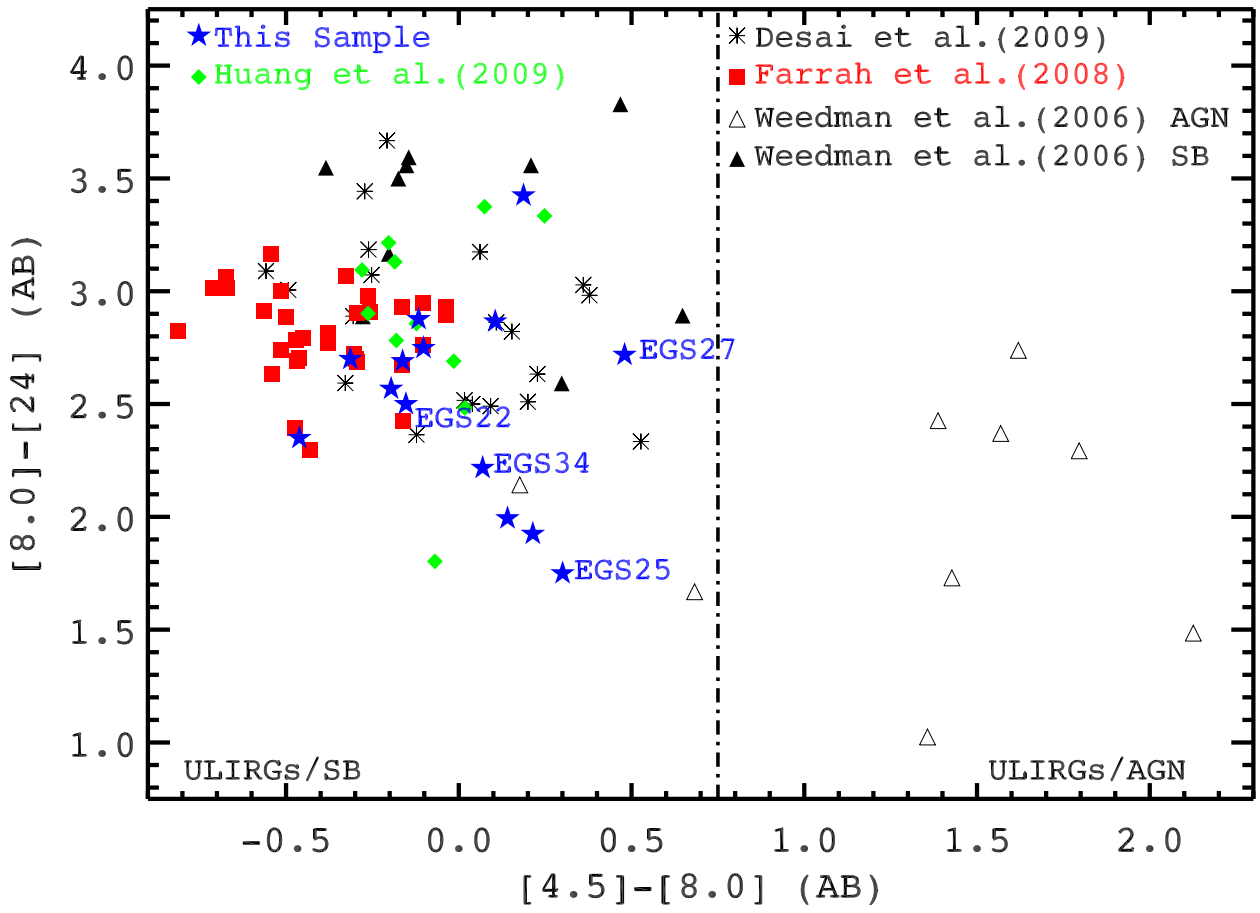

Fig. 13.— *Spitzer* color-color diagram. Points denote ULIRGs from various $z \sim 2$ spectroscopic samples as indicated in the figure legend. The four X-ray-detected objects in the present sample are labeled. The dot-dashed line ($[4.5] - [8.0] = 0.75$) was adopted from Pope et al. (2008).

Table 1: IRS Observation Sample

Nickname[a]	EGSIRAC[b]	R.A.[c] J2000	Dec.[c] J2000	F(3.6 μm) μJy	F(4.5 μm) μJy	F(5.8 μm) μJy	F(8.0 μm) μJy	F(24 μm) μJy
EGS2	J142326.59+533457.9	14:23:26.60	+53:34:58.1	27.14±4.66	31.68±0.64	39.19±6.50	27.28±2.05	324.93±30.41
EGS3	J142255.06+533453.8	14:22:55.07	+53:34:53.7	27.69±2.86	33.26±0.45	36.73±2.15	29.88±1.73	422.85±10.05
EGS5	J142220.76+532920.1	14:22:20.80	+53:29:20.2	43.02±9.96	50.05±1.62	55.44±1.83	37.48±1.82	450.59±46.80
EGS6	J142327.26+532819.0	14:23:27.27	+53:28:19.4	65.34±1.41	67.68±0.99	78.46±2.12	82.45±2.08	485.50±12.20
EGS9	J142246.97+532025.9	14:22:46.96	+53:20:26.1	75.22±1.72	102.62±1.61	90.71±2.13	67.10±1.58	584.23±16.45
EGS19	J142118.10+531746.4	14:21:18.12	+53:17:46.3	35.78±1.06	46.31±0.63	53.79±1.74	38.67±1.32	411.70±35.83
EGS21	J141955.30+530323.2	14:19:55.30	+53:03:23.2	7.59 ±0.72	15.14±0.54	20.85±0.91	17.99±1.20	421.68±36.93
EGS22	J142038.49+525749.8	14:20:38.49	+52:57:50.0	32.66±4.76	42.01±0.69	46.42±1.00	36.49±2.52	364.91±52.45
EGS25	J141947.52+525026.2	14:19:47.51	+52:50:26.2	62.22±0.48	68.35±0.37	59.24±1.13	90.15±1.13	451.84±16.20
EGS27	J141935.69+525109.0	14:19:35.71	+52:51:09.0	20.12±0.99	25.50±0.95	35.02±1.34	39.67±1.31	485.05±12.93
EGS32	J141835.11+524933.9	14:18:35.12	+52:49:33.7	21.68±1.39	29.83±0.47	38.10±1.50	33.97±1.35	213.10±15.26
EGS34	J141833.21+524241.8	14:18:33.19	+52:42:42.0	36.69±1.68	49.81±0.78	50.23±0.99	53.08±1.50	409.06±40.66
EGS48	J141601.52+521550.0	14:16:01.53	+52:15:50.0	24.22±2.80	33.97±0.26	41.72±0.97	37.44±1.12	524.55±18.09
EGS49	J141603.66+522122.6	14:16:03.69	+52:21:22.7	33.38±1.02	42.19±0.61	52.75±1.80	38.40±1.24	482.82± 8.22

[a]Nicknames are the target names in the *Spitzer* archive and are used for convenience in this paper, but they are not official names and should not be used as standalone source identifications.

[b]Source name from Barmby et al. (2008).

[c]R.A. and Dec. are the commanded telescope pointing coordinates, which differ by no more than 0.″33 from coordinates given by Barmby et al. (2008). For each observation, the telescope was pointed to the commanded coordinates by high accuracy peakup on nearby *2MASS* catalog stars observed on the blue peakup array.

Table 2: IRS Sample Selection Criteria.

Sample	F(24 μm) (mJy)	Color criteria
Houck et al. (2005)	>0.75	$\nu F_\nu(24\ \mu\mathrm{m})/\nu F_\nu(I) > 60$
Yan et al. (2007)	>0.90	$\nu F_\nu(24\ \mu\mathrm{m})/\nu F_\nu(I) > 10$ & $\nu F_\nu(24\ \mu\mathrm{m})/\nu F_\nu(8\ \mu\mathrm{m}) > 3.16$
Weedman et al. (2006)	>0.90	$F(\mathrm{X})^{\mathrm{a}} \gtrsim 10^{-15}$ erg cm^{-2} s^{-1}
Weedman et al. (2006)	>0.90	IRAC flux density peak at either 4.5 or 5.8 μm (SB)
Desai et al. (2009) (D09)	>0.50	$R-[24] > 14$ Vega mag and a strong rest-frame 1.6 μm bump in their IRAC SEDs
Farrah et al. (2008) (Far08)	>0.50	IRAC flux density peak at 4.5 μm
Fiolet et al. (2010) (Fio10)	>0.50	IRAC flux density peak at 5.8 μm
Fadda et al. (2010) (Fad10)	>0.14	24 μm sources fainter than 0.5 mJy
Huang et al. (2009) (H09)	>0.60	$0.05 < [3.6]-[4.5] < 0.4$ & $-0.7 < [3.6]-[8.0] < 0.5$
This paper	>0.20	$0 < [3.6]-[4.5]$ & $[5.8]-[8.0] < 0$

[a] *Chandra* 0.3–8 keV flux density

Table 3: Spectroscopic redshifts and $L_{\rm IR}$

Nickname	Redshift[a] (SB)	Redshift[a] (ULIRG)	$L(8\ \mu\mathrm{m})$[b] ($\mathrm{L}_\odot$)	$L_{\rm IR}$[c] ($\mathrm{L}_\odot$)	$L_{\rm IR}$[d] ($\mathrm{L}_\odot$)	SFR[e] ($\mathrm{M}_\odot$/yr)	$F(0.5-10\ \mathrm{keV})$[f] erg cm^{-2} s^{-1}
EGS2	1.97±0.08	1.95±0.02	11.41	12.38±0.35	12.05±0.27	410±140	-
EGS3	1.81±0.02	1.79±0.08	11.47	12.44±0.08	12.10±0.06	480±90	-
EGS5	1.95±0.03	1.92±0.06	11.55	12.52±0.24	12.16±0.19	570±190	-
EGS6	1.91±0.01	1.90±0.02	11.56	12.53±0.06	12.17±0.05	590±90	-
EGS9	1.79±0.02	1.77±0.05	11.62	12.59±0.08	12.22±0.07	680±130	-
EGS19	2.02±0.03	2.01±0.08	11.54	12.52±0.21	12.16±0.17	570±190	-
EGS21	2.01±0.04	1.94±0.10	11.55	12.52±0.24	12.16±0.19	570±190	-
EGS22	1.98±0.05	1.94±0.10	11.47	12.44±0.35	12.10±0.28	470±160	7.7×10^{-16}
EGS25	1.65±0.03	1.63±0.05	11.59	12.57±0.08	12.20±0.06	640±110	1.7×10^{-15}
EGS27	2.31±0.05	2.29±0.09	11.79	12.77±0.16	12.36±0.12	1020±370	1.7×10^{-15}
EGS32	2.36±0.05	2.34±0.12	11.44	12.41±0.24	12.07±0.18	440±150	-
EGS34	1.76±0.02	1.48±0.11	11.47	12.44±0.17	12.10±0.13	470±180	5.7×10^{-16}
EGS48	1.89±0.03	1.90±0.06	11.58	12.56±0.13	12.19±0.10	630±180	-
EGS49	1.91±0.04	1.90±0.07	11.56	12.53±0.13	12.17±0.10	580±170	-

[a] Redshifts obtained with a starburst (M82) or ULIRG (Arp 220) template as indicated.

[b] The rest-frame luminosity $L(8\ \mu\mathrm{m})$.

[c] $L_{\rm IR}$ obtained from $L(8\ \mu\mathrm{m})$ with the Caputi et al. (2007) relation.

[d] $L_{\rm IR}$ obtained from $L(8\ \mu\mathrm{m})$ with an empirical relation from Bavouzet et al. (2008) equation 7.

[e] SFRs from the Caputi et al. (2007) relation and the calibration by Kennicutt (1998): $\mathrm{SFR}\,(M_\odot\ \mathrm{yr}^{-1}) = 4.5\times10^{-44} L_{\rm IR}(\mathrm{erg\,s}^{-1})$.

[f] Four objects in our sample, EGS22/EGS25/EGS27/EGS34, are X-ray sources in the Chandra 800 ks AEGIS-X catalog.